

Politecnico of Turin



**Politecnico
di Torino**

Master's degree in Nanotechnologies for ICTs

Ion exchange membranes for energy applications

Supervisors:

Prof. Andrea LAMBERTI

Dr. Luisa BAUDINO

Dr. Michel SAAKES

Candidate:

Maria Antonietta LOPARDO

March 30, 2025

Abstract

The increasing energy demand has led to excessive greenhouse gas emissions, contributing to climate change. Greenhouse gases, especially carbon dioxide, are key drivers of global warming, and fossil fuels account for over 50% of global energy production. However, fossil fuels have significant drawbacks, including CO_2 emissions, finite supply, and dependence on unreliable imports. As a result, there is a global push to research and develop alternative, climate-neutral fuels to replace fossil fuels.

To address these environmental challenges, membrane technologies have emerged as promising solutions. These technologies rely on selective permeability, allowing only specific molecules or ions to pass through. Ion Exchange Membranes (IEMs) are a specific type of membrane which allow the passage of ions, while blocking co-ions. IEMs are increasingly being explored for innovative applications in energy conversion and production, which can be classified into water-based applications and energy-based applications. This thesis investigates an application of each type: Reverse ElectroDialysis (RED) as an energy production method starting from seawater and Direct SeaWater Electrolysis (DSWE) for green hydrogen generation.

The thesis begins by discussing various methods for blue energy harvesting, focusing on reverse electro-dialysis, and on the materials used in IEMs. Graphene-based IEMs reinforced with aramid fibers to enhance mechanical performance were used for this application. Different Graphene Oxide (GO) and fiber concentrations were investigated to evaluate their impact on the membrane properties. The membranes were then characterized morphologically, physicochemically and electrochemically, in terms of permselectivity and ionic resistance.

The potential of DSWE as an innovative approach for green hydrogen production was then addressed. A detailed overview of the materials used in fabricating for the IEMs and catalysts for the electrolysis process was provided and the performance of a commercial bipolar membrane for this kind of application was then evaluated. Special emphasis was placed on optimizing the cathode-side catalyst for the Hydrogen Evolution Reaction (HER) of the experimental setup and exploring different deposition techniques and substrate materials at Wetsus, the European Center of Excellence for Water Technology in Leeuwarden, The Netherlands.

Finally, the future scalability of membrane fabrication was discussed, including the potential of roll-to-roll processes, and prospects for meeting the European Union's targets for sustainable hydrogen production through DSWE, such as using asymmetric bipolar membranes.

Contents

1	Introduction	8
1.1	Blue energy	8
1.2	Direct Seawater electrolysis for hydrogen production	12
1.2.1	Bipolar membranes	13
1.2.2	BPM electrolysis basic set-up	15
1.2.3	Modified DSWE System with Integrated Electrocatalysts	16
2	Materials and Methods	18
2.1	GO membranes for blue energy applications	18
2.1.1	GO membrane materials	18
2.1.2	GO membrane fabrication	18
2.1.3	GO membrane characterizations	19
2.2	Bipolar Membranes for DSWE	23
2.2.1	DSWE system materials	23
2.2.2	Initial DSWE system	24
2.2.3	DSWE characterizations	30
3	Results and Discussion	33
3.1	GO membranes for blue energy applications	33
3.1.1	GO membranes fabrication	33
3.1.2	GO membrane characterizations	34
3.1.3	Scaling up trial	39
3.2	Bipolar membranes for DSWE	40
3.2.1	DSWE system characterizations	40
4	Conclusions	58
5	Appendix	61

List of Figures

1	Configurations of the three main technologies for harvesting blue energy [3].	9
2	RED technology configuration [1].	9
3	Working principle of IEMs [9].	10
4	Aramid fibers in PARA (Kevlar TM) and META (Nomex TM) configuration.	12
5	BPM in (a) reverse bias mode; (b) forward bias mode [20]. The yellow region represents the alkaline environment of the Anion Exchange Layer (AEL), which allows the passage of negative ions (X^-), while the blue region corresponds to the acid environment of the Cation Exchange Layer (CEL), which allows the passage of positive ions (M^+). The AEL/CEL interface region is the Intermediate Layer (IL), where water dissociation, represented by the gray arrows, occurs.	14
6	Osmosis cell working principle. Pure water passes as a gas from the 0.5M <i>NaCl</i> as artificial seawater to the catholyte thanks to difference water vapor pressure between seawater and catholyte.	17
7	Dead-end filtration set-up.	19
8	Schematics of the side-by-side cell used for the (a) permselectivity and (b) ionic resistance measurements. Dark blue and light blue represent solutions with different concentrations [25].	20
9	Examples of (a) OCP, (b) IV potentiostatic, and (c) VI galvanostatic measurement to calculate the open circuit voltage.	21
10	Examples of (a) EIS, (b) IV potentiostatic, and (c) VI galvanostatic measurements to calculate the ionic resistance.	22
11	(a) Titanium fiber felt (10cm x 10cm) coated with <i>Ir</i> -MMO ($10g/m^2$) for the anode; (b) titanium mesh (10cm x 10cm) coated with Pt ($60g/m^2$) for the cathode.	23
12	Schematics of the hybrid set-up for direct seawater electrolysis using a bipolar membrane electrolysis cell combined with an osmosis cell to extract pure water from 0.5M <i>NaCl</i> used as artificial seawater. Blue lines correspond to the catholyte (Na_2SO_4), yellow lines to the artificial seawater (<i>NaCl</i>), and red lines to the anolyte (<i>NaOH</i>). Green and pink lines represent the hydrogen and oxygen gases generated.	25
13	Hybrid set-up for direct seawater electrolysis using a bipolar membrane electrolysis cell combined with an osmosis cell to extract pure water from 0.5M <i>NaCl</i> as artificial seawater.	26
14	Schematics of the configuration of the bipolar membrane electrolyser cell. The HER and OER catalysts are represented by the orange layers, while the Porous Transport Layers (PTLs) correspond to the green regions. At the AEL/CEL interface there is the BPM junction, depicted in blue, where the water splitting reaction occurs. The current collectors at the anode and cathode side are reported in gray. The porous Teflon membrane of the osmosis cell is reported on the cathode side.	27

15	Electrolyser cell (10cm x 10cm): (a) Anode side; (b) Cathode side.	27
16	System used for the Ultraturrax-assisted coating of sintered nickel felt with <i>NiFeCo</i> electrocatalyst, showing the Ultraturrax at 20000rpm and the integrated ice bath. . .	29
17	System used for the vacuum-assisted coating of <i>NiFeCo</i> on the sintered nickel felt substrate, showing the vacuum pump and the Buchner funnel containing the filter. .	30
18	Fabricated membranes: (a) used concentrations of GO and ANF; (b) photos of the membranes after the drying.	34
19	FESEM analysis of different membranes. (a) 10mg GO with 25% ANF; (b) 10mg GO with 25% ANF after the OCP measurement; (c) 10mg GO with 50% ANF.	35
20	FTIR spectra of GO (blue), aramid fibers (red) and of the membrane containing 15mg GO and 25% ANF (black).	36
21	Open circuit voltage evolution over time for the four composite membranes. All the values have been corrected with the corresponding blank measurements.	37
22	(a) Potentiostatic current-voltage (IV) and (b) galvanostatic voltage-current (VI) analyses of composite membranes with varying aramid nanofibers concentrations. Increasing ANF content while maintaining constant GO mass resulted in increased ionic resistance. This trend is demonstrated by a steeper linear regression slope in the IV curve and a reduced slope in the VI curve.	38
23	(a) OCP and (b) ionic resistance values the four membranes. Error bars correspond to the standard deviation of each value. All the values have been corrected with the corresponding blank measurements.	39
24	Schematics of the roll-to-roll process [29].	40
25	SEM images of the sintered nickel felt coated with a dispersion of <i>NiFeCo</i> with Nafion, 2-propanol and SDS using the Ultraturrax-assisted coating method.	41
26	Dispersion of <i>NiFeCo</i> with Nafion, 2-propanol and SDS used for the Ultraturrax-assisted coating method. The nanoparticles tended to precipitate at the bottom of the container.	41
27	Cross sections SEM images of the sintered <i>Ni</i> -felt coated with the <i>NiFeCo</i> dispersion using the Ultraturrax-assisted coating method. Images show (a) the top, (b) central, and (c) bottom regions of the coated material.	42
28	(a) Photo and (b) SEM image of <i>Ni</i> -felt coated with <i>NiFeCo</i> using vacuum-assisted filtration method.	42
29	(a,b) Sintered <i>Ni</i> -felt coated with <i>NiFeCo</i> using dip-coating, (c) Sintered <i>Ni</i> -felt coated with <i>NiFeCo</i> using dip-coating submerged in water. No detachment is visible.	43
30	SEM images of the <i>Ni</i> -felt coated with <i>NiFeCo</i> using dip-coating method: (a) top view and (b) cross section.	43
31	<i>Ni</i> -foam (10cm x 10cm) partially coated with <i>NiFeCo</i> (right side) using dip-coating. The partial coating, highlighted by the color change, that occurred was due the absence of oxygen due to sealing flat PP container with Parafilm tape. However, the presence of oxygen gas appeared essential for the electrochemical reactions to occur.	44
32	SEM images of the <i>Ni</i> -foam coated with <i>NiFeCo</i> TLH catalyst using dip-coating method: (a) top view and (b,c) cross section. The dip coating process lasted at least one week.	45

33	Voltage drop across the Fumatech BPM at $1000A/m^2$. The blue lines are the measured potential difference across the bipolar membrane at $1000A/m^2$ using two different reference electrodes ($Ag/AgCl$ (3M KCl) and Hg/HgO (1M KOH)). In contrast, the red lines show the corrected potential difference across the Fumatech BPM at $1000A/m^2$. The anolyte was 1M $NaOH$ solution at the start, while the catholyte was 1M Na_2SO_4 solution at the start. During electrolysis, the concentration of the anolyte and catholyte increased due to the consumption of water during electrolysis.	48
34	(a) Anode and cathode potentials after the run at $1000A/m^2$ of the electrolyser cell with five layers of titanium fiber felt ($175\mu m$) coated with $10g/m^2$ Ir -MMO at the anode and five layers of titanium mesh ($150\mu m$) coated with $60g/m^2$ of platinum at the cathode (second test). Anode potential was stable around 1.0V, while the cathode potential exceeded the recording limit of IVIUM software of $-2V$; (b) autopsy of the instable bipolar membrane electrolysis cell of the second test. BPM showed wrinkling after the run.	49
35	Black-colored platinized $150\mu m$ Ti -mesh due to a high pH at the cathode side.	49
36	Evolution of cell voltage over time for different cathode compositions of the electrolyzer cell. (a) Pure nickel foam without electrocatalyst; (b) Thin platinized titanium mesh; (c) Ultraturrax $NiFeCo$ nanoparticle dip; (d) $NiFeCo$ coating in Buncher funnel; (e) Dip coating Ni -felt (Ni,Fe,Co) Cl_2 ; (f) Dip coating Ni -foam (Ni,Fe,Co) Cl_2	52
37	Comparison of cell voltage and voltage efficiency for different cathode side configuration. Error bars represent standard deviation across multiple experimental runs, except for the <i>Buchner funnel</i> method, which was conducted only once.	53
38	Evolution of the (a) anode potential and (b) cathode potential vs Hg/HgO (1M KOH) over time for the different electrolyser cell configuration. The data reported correspond to the fourth run for each experiment.	55

List of Tables

1	Comparison of Reverse Electrodialysis (RED), Pressure Retarded Osmosis (PRO), and Capacitive Mixing (CapMix) technologies. The table summarizes their operational mechanisms, achieved power densities, and up-scaling possibilities [6] [7] [8].	10
2	Fabrication parameters and corresponding filtration and drying time for the membranes containing 10 mg of graphene oxide and a different ANF content.	33
3	Open circuit voltages values for the four membranes calculated as an average of a 15 minutes OCP measurements. Two blank measurements are necessary because two solutions are used. The OCP membrane is calculated as equation (3.1).	36
4	Ionic resistance measured values for the four membranes derived from EIS, IV potentiostatic, and VI galvanostatic measurements. All the values have been corrected with the corresponding blank measurements.	37
5	Open circuit voltage, permselectivity and ionic resistance measured values for the four membranes. Ionic resistance is calculated as the average of values derived from EIS, IV potentiostatic, and VI galvanostatic measurements. All the values have been corrected with the corresponding blank measurements.	38
6	Parameters used for the GO condensation and final concentrations.	40
7	EDX spectrum of (a) nickel felt and (b) nickel foam coated with <i>NiFeCo</i> using the dip-coating method.	46
8	Summary of the elemental composition obtained from the EDX analysis for <i>Ni</i> -felt and <i>Ni</i> -foam substrates. The reported mass values were used to calculate the molar fractions of <i>Co</i> , <i>Fe</i> and <i>Ni</i> in the TLH catalyst deposited on each substrate. The calculated molarity of each element is also included.	47
9	Summary of four-hour test results for the six electrolyser cell configurations carried out at $1000A/m^2$ for bipolar membrane electrolysis controlled at 30.0 °C for different methods for coating the catalyst for the HER at the cathode. Each row represents the average value of four runs for an electrolyser cell configuration characterized by the electrocatalyst applied at the cathode. The table reports the measured cell potentials and BPM potentials.	50
10	Summary of four-hour test results for the six electrolyser cell configurations carried out at $1000A/m^2$ for bipolar membrane electrolysis controlled at 30.0 °C for different methods for coating the catalyst for the HER at the cathode. Each row represents the average value of four runs for an electrolyser cell configuration characterized by the electrocatalyst applied at the cathode. The table reports the anode and cathode potential vs <i>Hg/HgO</i> (1M <i>KOH</i>) reference electrode.	51
11	Cathode and anode overpotential calculated according to equation (3.27) and (3.31) and assuming water reduction at the cathode. Condition: $1000A/m^2$ and operated at 30.0 °C in 1M <i>Na₂SO₄</i> at pH = 13.4	57

-
- 12 Comparison of cell potentials in alkaline water electrolysis and bipolar membrane systems. The AWE cell potential is calculated as the difference between the anode and cathode potentials of the DSWE system with BPM, while the BPM cell potential includes the additional contribution of the membrane potential. 57

Introduction

The growing energy demand has led to excessive greenhouse gas emissions and climate change. This situation has driven research communities to seek out renewable energy sources that are affordable, efficient, and reliable to replace fossil-fuel-based technologies. Blue energy, known as salinity-gradient energy, has recently gained attention in research and development. It exploits the osmotic energy generated by the salinity gradients between seawater and freshwater, relying on the Gibbs free energy released when two solutions with different salinity levels mix. Thus, blue energy does not produce significant greenhouse gas emissions or suffers from intermittency issues. This process is driven by the increase in system entropy without any change in enthalpy [1].

In parallel, hydrogen is emerging as a potential energy carrier that can be used to decarbonize our energy system. However, 96% of hydrogen production currently relies on fossil fuels [2], through steam methane reforming of natural gas or coal gasification, thus contributing to carbon emissions. The hydrogen produced using these non-sustainable methods is referred to as *gray hydrogen*. To integrate hydrogen into a carbon-free energy system, sustainable production methods must be developed. A possible solution to produce hydrogen using environmentally friendly methods is to use water electrolysis, which splits water into oxygen and hydrogen using renewable electricity. In this case, if the current is supplied using renewable energies, the hydrogen is commonly known as *green hydrogen*. However, water electrolysis requires high-purity water, which is challenging in terms of freshwater consumption and desalination methods. To address this limitation, Direct SeaWater Electrolysis (DSWE) is being investigated. DSWE is an advanced method to produce green hydrogen directly from seawater without the need for desalination.

1.1 Blue energy

Blue energy, based on the osmotic energy generated by the salinity gradient between two solutions with a different salinity concentration, is a type of renewable energy that is considered secure, scalable, reliable and, most importantly, constant.

The three main technologies for blue energy harvesting are Pressure Retarded Osmosis (PRO), Reverse Electrodialysis (RED), and Capacitive Mixing (CapMix) (figure 1). Some of these are membrane-based, while others may incorporate a membrane, although not in their standard configuration. The role of these membranes is crucial: they prevent the mixing of high-salinity and low-salinity solutions, thereby maintaining the salinity gradient necessary for energy generation. The most used membranes for this kind of applications are Ion Exchange Membranes (IEMs). IEM is a semi-permeable membrane which permits the selective passage of ions while blocking others. They can either be Cation Exchange Membranes (CEM), which allow positive ions to pass, or Anion Exchange Membranes (AEM), which allow negative ions to pass.

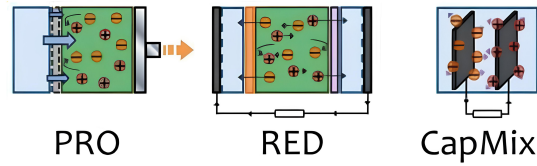


Figure 1: Configurations of the three main technologies for harvesting blue energy [3].

In the case of Pressure Retarded Osmosis (PRO), a low-salinity solution and a pressurized high-salinity solution are separated using a water-permeable membrane, creating osmotic pressure. The membrane allows the transport of the solvent of the lower concentrated solution, such as river water, toward the high concentrated solution, like seawater. The osmotic pressure is then converted into mechanical energy to drive hydro-turbines and generate electrical power [4]. The efficiency of this technology is highly dependent on the properties of the membrane, mostly on its permeability. In fact, the efficiency of the system can be greatly reduced by the permeation of salts into the membrane. Using PRO, it is possible to generate 1MW for one cubic meter per second of freshwater that flows through the membrane [1], however, developing a high performance and a solute-impermeable membrane is fundamental to the generation of high efficiency PRO power plants.

In Reverse Electrodialysis (RED), an IEM is placed between two streams of different salinity, allowing ions to flow from the most concentrated stream to the less concentrated one. This ions flow between the two sides of the membrane creates a potential difference. Redox couples at the current collector convert the ion flow into an electrical current flow which runs in the external circuit [5]. In figure 2, a stacks of alternating anion-exchange membranes and cation-exchanges membranes for RED application, is reported. The opposite movement of anions and cations across the AEM and CEM, according to their concentration gradients, creates a net charged ion flux.

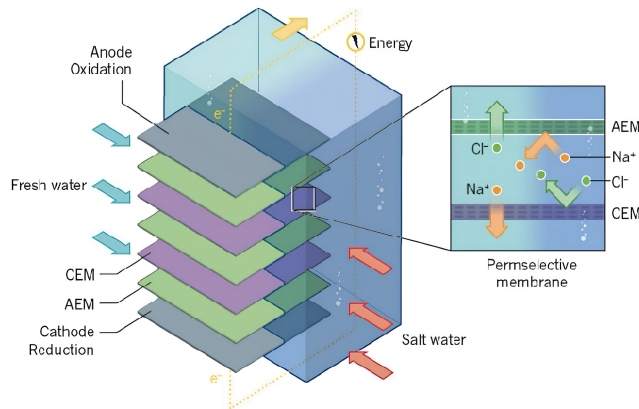


Figure 2: RED technology configuration [1].

On the other hand, Capacitive Mixing (CapMix) typically operates without membranes, using two porous electrodes submerged in alternating high- and low-salinity solutions. Usually, an intermediate washing step is included between solution exchanges to prevent contamination. The capacitance of these electrodes shifts as the solutions are exchanged: exposure to high-salinity water charges the electrodes, while immersion in low-salinity water lowers their potential, enabling discharge. In the basic CapMix configuration, the electrodes charge or discharge through the surface accumulation of charges from the solution to the electrode. This charge-discharge cycle can be used to capture and convert this energy into electricity [6]. The addition of an IEM leads to the Capacitive Donnan potential configuration of the CapMix technology, which takes advantage of the Donnan potentials. This

potential is an electrochemical potential that develop across such membranes due to the imbalance of mobile ions across a charged membrane, restricting the permeation of co-ions.

Table 1 summarizes the working principle, power densities and the scalability of RED, PRO and CapMix. Reverse electro dialysis is widely regarded as the most promising salinity energy technology thanks to its balance of efficiency (high power density), scalability, and technological maturity. In contrast, CapMix has a lower power density compared to the other technologies and limited scalability due to the degradation of the electrodes over repeated cycles. However, research is exploring innovative solutions, such as parallel electrode connections, to address these limitations and enable up-scaling of this technology.

Table 1: Comparison of Reverse Electro dialysis (RED), Pressure Retarded Osmosis (PRO), and Capacitive Mixing (CapMix) technologies. The table summarizes their operational mechanisms, achieved power densities, and up-scaling possibilities [6] [7] [8].

Technology	Mechanism	Achieved power density	Scalability
PRO	Osmosis drives water from the low-salinity solution to the high-salinity solution, generating osmotic pressure that is converted into mechanical energy	2.3-38 W/m^2	limited scalability due to fouling and mechanical stress
RED	Ion-exchange membranes create an electric potential via an ion concentration gradient.	0.77-1.2 W/m^2	high scalability thanks to low resistance membranes and modular design
CapMix	Electricity is generated through charge and discharge cycles of porous electrodes immersed in solutions with different salinity levels	0.007 - 0.2 W/m^2	parallel electrode configuration is promising

As highlighted in the table 1, the most used membranes in the case of reverse electro dialysis technology are Ion Exchange Membranes (IEMs). IEMs are semi-permeable membranes which permit the selective passage of certain ions while blocking others. These membranes are divided into two categories, according to the type of ions that are allowed to pass through. Cation Exchange Membranes (CEM) allow only the passage of cations, since they possess anionic groups on the surface (e.g., sulfonate $-SO_3^-$ or carboxylate $-COO^-$). On the other hand, Anion Exchange Membranes (AEM) do not allow cations to pass through the membrane, due to the presence of cationic groups (e.g., quaternary ammonium $-NR_3^+$) on their surface (figure 3).

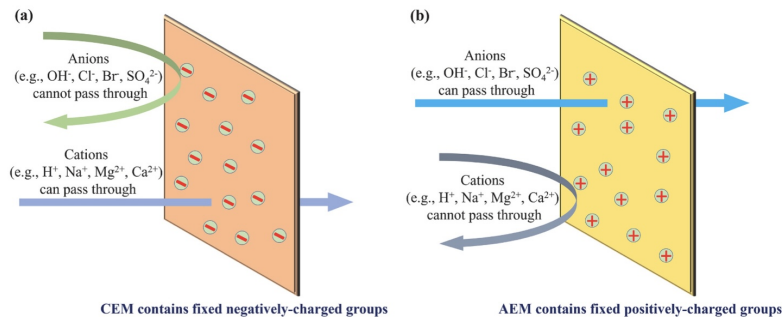


Figure 3: Working principle of IEMs [9].

Thanks to their ability to maintain ionic separation under electrical potential gradients, these membranes are critical in applications such as water desalination, fuel cells, and electrodialysis. However, their fabrication may include the use of materials with high environmental impact. For example, synthetic polymers, often derive from petrochemicals [10]. Thus, it is important to develop environmentally friendly methods for membrane fabrication.

Selecting the appropriate membrane requires tuning its properties with the specific demands of the future application, since different technologies prioritize distinct characteristics [9]. Ideally, IEMs should possess high permselectivity and thermal and mechanical stability, as well as low ionic resistance. Permselectivity is the membrane's ability to preferentially transport counter-ions, which are ions of charge opposite to the fixed groups, while blocking co-ions, which share the same charge as the surface groups. High permselectivity is achieved through a dense distribution of functional groups. However, achieving ideal permselectivity of 100% remains challenging due to practical limitations such as membrane imperfections and swelling under operational conditions. Similarly, Ionic resistance describes the resistance offered by the IEM to the movements of ions through it.

Mechanical and thermal stability are also vital for IEMs, particularly in demanding industrial applications. To increase the mechanical stability, a reinforcement may be added to the membrane, making it thicker. However, thin membranes exhibit lower electrical resistance compared to thicker membranes, thus a trade-off must be found.

Traditional polymeric membranes face challenges such as performance reduction in highly concentrated or multivalent solutions and a higher degree of swelling [11]. Thanks to the large variety of polymers which can be used as matrix for the membrane, different properties and characteristics can be obtained. For example, membranes with high porosity can usually have large conductivity [12]. The most used polymers as matrix for the polymeric membranes are polystyrene, polypropylene and polyethersulfone [13]. IEMs can also be made from inorganic materials, such as zeolites, which offer better thermal stability. However, they are generally more expensive and may exhibit lower electrochemical performance in certain applications [14].

The recent development of two-dimensional (2D) materials, such as graphene and its derivatives, offers a promising alternative to compensate the ionic resistance-permselectivity trade-off. These new materials address the limitations of traditional membranes and pave the way for more efficient and sustainable ion-exchange technologies.

Graphene oxide

Graphene Oxide (GO) is a two-dimensional material derived from oxidized graphene sheets. It is functionalized with oxygen-containing groups such as hydroxyl ($-OH$), carboxyl ($-COOH$), and epoxy ($-O-$) groups, which confer hydrophilic properties. GO exhibits a combination of mechanical strength (130GPa tensile strength), large surface area (2630m²/g) and tunable electrical conductivity [15]. Moreover, the lamellar structure of GO allows precise control over interlayer spacing (typically 0.6–1.2nm), enabling size-selective ion transport, while its intrinsic negative surface charge allows cation selectivity.

Graphene oxide represent a promising alternative for the production of green membranes if produced with environmentally friendly methods. GO can be used in CEM thanks to the negative charge intrinsically present on its surface. However, it can be easily functionalized in order to obtain AEM. GO membranes have several advantages compared to traditional polymeric membranes, thanks to the large surface area, mechanical strength and electrical conductivity of the graphene oxide. Their stacked nanosheet structure creates nanochannels for rapid ion transport (low resistance) while maintaining charge-selectivity (high permselectivity). Furthermore, GO's mechanical robustness allows thinner membrane designs (10μm) compared to conventional IEMs (50–200μm), reducing overall resistance while maintaining durability.

However, its current fabrication method relies mainly on energy-intensive methods, which include the use of harsh chemicals and toxic by-products, therefore it is important to develop a green method for its future large-scale application [10].

To enhance the mechanical strength of GO-based membranes, reinforcements such as Aramid NanoFibers (ANFs) can be incorporated in the composite membrane. Aramid nanofibers are composed of aromatic benzene rings linked by amide ($-CO-NH-$) bonds. According to the position of these bonds on the benzene rings, aramid fibers are categorized in Para (Kevlar[™]) configuration, if the bonds are opposite, and Meta (Nomex[™]) configuration, in which the bonds are adjacent and attached to the ring at carbons 1 and 2 [16]. These different configurations are reported in the figure 4. Nomex fibers, made of poly(m-phenylene isophthalamide), have a zig-zag meta-configuration, which reduces tensile strength but enhances flexibility. These fibers are used as reinforcement in membrane fabrication thanks to their thermal stability, resistance, and high mechanical strength.

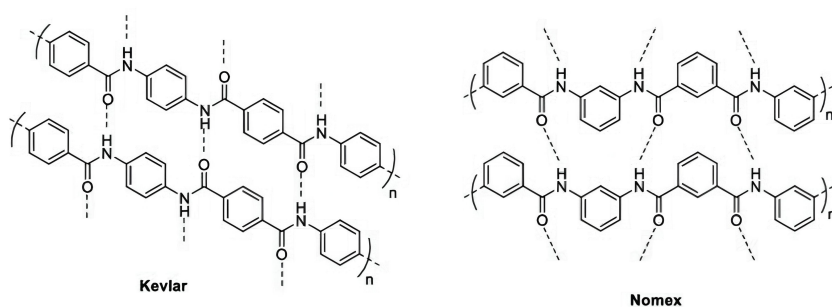


Figure 4: Aramid fibers in PARA (Kevlar[™]) and META (Nomex[™]) configuration.

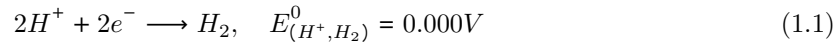
1.2 Direct Seawater electrolysis for hydrogen production

As global energy demands continue to rise, hydrogen is emerging as a critical energy carrier and a promising alternative to fossil fuels. Its versatility allows for applications including transportation, industrial processes, and energy storage. To realize the full potential of hydrogen, environmentally sustainable production methods must be employed. Proton Exchange Membrane Electrolysis (PEME) and Alkaline Water Electrolysis (AWE) are established environmentally friendly technologies for producing hydrogen from water. However, both PEME and AWE systems rely on high-purity water as a feedstock.

While desalination of seawater to provide pure water is not prohibitive in terms of energy or cost [17], it does require regular maintenance and creates large amounts of highly saline waste concentrates, which are difficult to dispose of, so it is preferable to avoid it. Moreover, as hydrogen demand scales up for future use to more than 7Mt for Europe, resource shortages in using pure water from drinking water may arise [18]. An emerging alternative to avoid desalination to make ultra-pure water is Direct Seawater Electrolysis (DSWE). DSWE represents an attractive route to sustainable hydrogen production, as it directly uses seawater, an almost infinite resource of constant and reliable water.

The electrolysis of water involves two key electrochemical reactions: the Hydrogen Evolution Reaction (HER) at the cathode and the Oxygen Evolution Reaction (OER) at the anode. The HER is a two-electron process that generates molecular hydrogen, while the OER is a four-electron process that produces molecular oxygen. The HER and OER reactions are respectively represented by the

following equations vs Normal Hydrogen Electrode (NHE):



where E^0 is the standard redox potential of the corresponding reaction which indicates the tendency of a redox couple to undergo reduction or oxidation and it is defined under standard conditions: 298 K, 1 atm pressure (for gases), and 1M concentration (for solutions).

Thermodynamically, to induce water splitting a 1.23V theoretical voltage is required, but in practice the reaction is triggered by a larger potential. This is because the two reactions have large activation barriers, leading to an excess potential for the overall water splitting, referred to as overpotential. This overpotential contributes significantly to the energy consumption of the electrolysis process. Each electrochemical reaction has distinct requirements influenced by the surface pH conditions at each electrode.

The European Union target for Direct Seawater Electrolysis (DSWE) is to operate at a current density of $5000A/m^2$ with a cell voltage of 2.0V under isothermal conditions, specifically within a temperature range of 50–60 °C. However, this study maintains a constant temperature of 30.0 °C as the Fumatech bipolar membrane should not operate above 40 °C.

Several configurations of electrolyser cells have been proposed for DSWE, but those utilizing bipolar membranes stand out due to their ability to sustain a pH gradient, enabling the water-splitting half-reactions to occur under their most kinetically favorable conditions[19].

In this study, a hybrid setup that includes a Bipolar Membrane (BPM) electrolyser and an osmotic cell is employed to realize an in situ self-driven water desalination and water electrolysis in a single system.

1.2.1 Bipolar membranes

A Bipolar Membrane BPM is a particular ion exchange membrane composed of a Cation Exchange Layer (CEL) and an Anion Exchange Layer (AEL) and a junction in between that contains a water-splitting catalyst. The water-splitting catalyst splits water into protons and hydroxyl ions. The AEL contains positive charges and is used to prevent cation transport, while the CEL contains negative charges and allows only cation passage. Consequently, anions and cations are not allowed to pass both layers of the BPM. Thus, when a current is applied, the flux is sustained by OH^- and H^+ ions, which are generated at the interface AEL/CEL.

The BPM can be used in two working conditions, according to the relative position of electrodes and BPM: reverse bias mode and forward bias mode (figure 5). In the reverse bias mode, the CEL faces the cathode, and the AEL faces the anode. OH^- ions are produced at the junction of the bipolar membrane and diffuse through the AEL, creating a high pH solution (alkaline environment, in yellow in figure 5). In contrast, H^+ ions produced at the junction of the bipolar membrane is transported through the CEL to produce an acid solution, depicted in blue in figure 5[19]. In forward bias mode, the opposite happens: H^+ and OH^- ions travel toward the interface, recombining into water and creating a low resistance condition for the BPM. In this case, the CEL faces the anode and the AEL faces the cathode [20].

Being composed of two layers, the overall BPM properties depend on the interface's and single layers' properties. The BPM must have high selectivity and low operating voltage; however, achieving high selectivity often conflicts with maintaining low operating voltages, leading to a trade-off in BPM design.

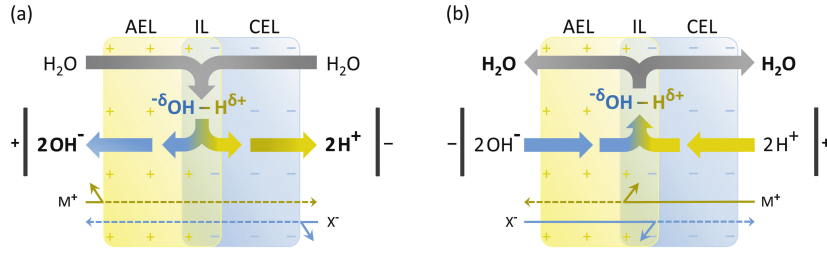


Figure 5: BPM in (a) reverse bias mode; (b) forward bias mode [20]. The yellow region represents the alkaline environment of the Anion Exchange Layer (AEL), which allows the passage of negative ions (X^-), while the blue region corresponds to the acid environment of the Cation Exchange Layer (CEL), which allows the passage of positive ions (M^+). The AEL/CEL interface region is the Intermediate Layer (IL), where water dissociation, represented by the gray arrows, occurs.

For water electrolysis applications, the Bipolar Membrane (BPM) must be operated in reverse bias mode to prevent the recombination of ions into water. This is achieved by maintaining the Cation Exchange Layer (CEL) at a lower potential than the Anion Exchange Layer (AEL) [21]. This potential difference drives the mobile H^+ and OH^- ions away from the BPM junction. The water reaches the junction of the bipolar membrane through diffusion, which must be ensured by a continuous supply of water in the electrolysis cell via the osmose membrane. The rate of diffusion of water towards the junction of the Bipolar Membrane should be high enough to avoid membrane dehydration and an unstable pH gradient [19] at the current density applied of $1000A/m^2$.

The BPM in reverse bias condition establishes a stable pH gradient across the BPM, with a higher pH on the AEL side (anode) and a lower pH on the CEL side (cathode).

In bipolar membrane water electrolysis, the Hydrogen Evolution Reaction (HER) has a theoretical onset potential of 0V vs Standard Hydrogen Electrode (SHE) at pH 0, while the Oxygen Evolution Reaction (OER) begins at +0.404V vs SHE at pH 14. However, the pH gradient introduces an additional voltage penalty due to the thermodynamic relationship between pH and potential [19]:

$$E_{pH} = 2.3 \frac{RT}{nF} \Delta pH = 0.059V \times \Delta pH = 0.826V \quad (1.3)$$

assuming $\Delta pH = 14$. The voltage penalty inherent to the pH gradient across a Bipolar Membrane (BPM) highlights the critical need for introducing oxygen and hydrogen evolution electrocatalysts. Electrocatalysts are catalysts that participate in electrochemical reactions, without consuming the catalyst itself during the reaction. They lower the activation energy of the reaction, i.e. the energy barrier that must be overcome before the reaction can take place, making the reaction faster, thus reducing the overpotential.

The stable pH gradient established across the BPM creates distinct environments at each electrode, necessitating electrocatalysts specifically optimized for these conditions. At the anode, hydroxyl ions (OH^-) are oxidized to oxygen in an alkaline environment, requiring catalysts optimized for high pH. Meanwhile, at the cathode, protons (H^+) are reduced to hydrogen in an acidic environment, demanding catalysts suited for low pH.

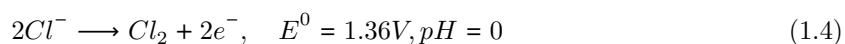
In this study, we assume a local pH equal or close to zero at the interface of the CEL layer of the bipolar membrane and the cathode and a local pH close to 14 at the interface of the AEL of the bipolar membrane and the anode.

1.2.2 BPM electrolysis basic set-up

The optimal approach to achieve zero-gap bipolar membrane electrolysis is to place the electrocatalyst layers directly at the surfaces of the bipolar membrane. However, due to the wet storage condition of the commercial bipolar membrane of Fumatech (Germany), used in this research, direct coating of the electrocatalyst on the surfaces of the bipolar membrane is not feasible. Instead, Porous Transport Layers (PTL) must be employed to apply the electrocatalyst layer to oxidize hydroxyl ions to oxygen and reduce protons to hydrogen. The PTL is a porous substrate that facilitates the transport of gases, specifically oxygen and hydrogen, and liquids. For optimal performance, the PTL must demonstrate high conductivity for either hydroxyl ions or protons and be stable against corrosion at the anode. The thickness of the PTL varies and is in the order of $50 - 1000\mu m$.

Seawater electrolysis offers several advantages in resource availability and cost-effectiveness compared to pure-water electrolysis. However, the complex ionic composition of seawater presents a significant challenge for this technology. These challenges are mainly related to chloride and other undesirable cations such as Mg^{2+} , Ca^{2+} , and Sr^{2+} , which are abundant in seawater. They are the reason of the limited use of electrolysis for hydrogen production, with currently only 4% hydrogen produced by this method [2]. Due to the predominance of Na^+ and Cl^- ions in seawater, researchers often employ a 0.5M $NaCl$ solution as a simplified model to simulate natural seawater in laboratory studies [22].

The presence of chloride ions in seawater will seriously hinder direct seawater electrolysis, especially for the OER process, that is a sluggish process as it is a four-electron transfer process, and relatively slow compared to HER, which is a dual-electron transfer process. Moreover, the chlorine evolution is faster and contributes to about 70% of the anode reaction while the other 30% is oxygen evolution at the anode. Because of its high concentration in seawater and low standard redox potential, Cl^- is considered the main competitor in the oxidation process because it can easily undergo a Chlorine Evolution Reaction (CER) in the electrochemical process. CER vs SHE is given by:



To overcome this issue, studies have shown that the pH must be higher than 7.5 in order to maximize the difference in the potential between the OER and the hypochlorite formation. This suggests that alkaline conditions are beneficial to OER. This is one of the reasons why the use of the BPM is crucial for direct seawater electrolysis. In fact, in contrast to setups employing only a Cation Exchange Membrane (CEM), the high local pH at the BPM anode interface inhibits OCl^- formation at the anode, mitigating the risk of undesired chlorine or hypochlorite generation. In contrast, using only a CEM would not create this high local pH at the anode, leading to OCl^- formation in pH-neutral anolyte conditions. However, BPM is not ideal, so it can allow some Cl^- flow from the cathode to the anode, which is unwanted because Cl^- should not be present on the anode side (forbidden Cl^- path). To overcome the co-ion transport of chloride, the bipolar membrane therefore is operated at a high current density of $1000A/m^2$. The applied current density is limited by the membrane's properties: exceeding this limit with the Fumatech BPM used in this research can cause membrane dehydration and failure.

There are different approaches for supplying water in the process of Bipolar Membrane Electrolysis:

- Seawater as the anolyte:

Introducing seawater directly at the anode poses several issues, particularly due to the complexation of non-passivated nickel (commonly used as the PTL of the electrolysis cell) with chloride anions during anodization at the AEL side of the bipolar membrane. The presence of these chloride ions, even in trace amounts, can cause corrosion of the Ni electrode during the anodization process because several complexes can be formed: $Ni(II)Cl^+$, $Ni(II)Cl_2^-$. One possible solution is to replace Ni with a noble metal like platinum (Pt). However, this is costly and less desirable. An alternative is to passivate first the Ni electrode in very pure alkaline

solution in advance to prevent corrosion of nickel in seawater. This is accomplished by using first ultrapure potassium hydroxide (KOH) solution, which forms a passivation layer on nickel during anodization, protecting it from unwanted reactions. NiO , $Ni(OH)_2$, and $NiOOH$ can be formed during this passivation. After this passivation step, we postulate that a pH-neutral electrolyte like sodium sulfate may be used as an anolyte. The local pH value at the AEL surface of the bipolar membrane (high pH) also high in the case of a pH-neutral bulk electrolyte while running the bipolar membrane in water-splitting conditions (producing acid and base at the junction of the bipolar membrane) at a high current density of $1000A/m^2$. Semiconductor-grade KOH is preferred as an anolyte for the passivation of pure nickel. However, being very expensive, standard KOH is purchased and purified first in-situ.

- Seawater as the catholyte (configuration used in this work):

When seawater is used directly as the catholyte, scaling (formation of insoluble precipitates on the cathode surface) can occur due to the presence of divalent cations like Ca^{2+} and Mg^{2+} ions, especially when a cation or anion exchange membrane is employed as the separator. During water reduction, hydroxyl ions and hydrogen gas are made at the cathode. This leads to scaling due to the formation of $CaCO_3$ and $MgCO_3$. To enable the use of seawater as the catholyte, a low local pH must be introduced at the surface of the electrocatalyst for the HER. This can only be accomplished by using a bipolar membrane. During the process of water splitting in the bipolar membrane, protons are generated at the surface of the cation exchange layer of the bipolar membrane. This approach uses the local low pH environment at the surface of the bipolar membrane where hydrogen gas is made via the reduction of protons at the porous transport layer containing the electrocatalyst for the Hydrogen Evolution Reaction (HER). This cell configuration with the bipolar membrane enables a very low local pH at the PTL for hydrogen gas formation and reduces scaling formation during the cathodic reaction, as the reaction now involves the reduction of protons to hydrogen gas rather than reducing water to hydroxyl ions and hydrogen gas. To further prevent scaling, it is necessary that the porous transport layer, which acts as a porous substrate for the electrocatalyst for the reduction of protons, has at least a porosity of 5% or more.

1.2.3 Modified DSWE System with Integrated Electrocatalysts

One of the primary objectives of this study is to reduce the overall cell voltage in a direct seawater electrolysis system using a hybrid set-up with bipolar membrane electrolysis cell combined with a osmose cell. To achieve this, electrocatalysts for OER and HER must be strategically integrated onto the porous transport layers at the interface of the bipolar membrane, enhancing reaction kinetics and minimizing overpotentials for OER and HER.

Due to the pH gradient generated across the bipolar membrane the conditions for the electrocatalyst for the oxidation of hydroxyl ions at the anode and the conditions of the electrocatalyst for the reduction of protons at the cathode are not identical, necessitating electrocatalysts that are specifically optimized for the unique pH environment of each electrode. Therefore, two different electrocatalysts must be added at the surface of the porous transport layer at the AEL of the BPM (anode) and the surface of the porous transport layer at the CEL of the BPM (cathode).

State of the art catalysts includes noble metals as HER catalyst. However, their high cost and low abundance prohibits large-scale implementation of noble metal catalyst in DSWE devices. Based on literature data, another possibility for the electrocatalysts and PTLs include earth abundant materials as electrocatalyst for the HER. For example, nickel-based HER catalysts, such as $NiFeCo$ alloys, are known to reduce the overpotential associated with the hydrogen evolution reaction, leading to increased catalytic activity. The enhanced catalytic performance is attributed to the interactions between the catalytic properties of Ni (low hydrogen overvoltage) and Co (high hydrogen absorption)

Materials and Methods

This section details the materials and methods employed in this research. Firstly, we describe the materials and procedures for fabricating the Graphene Oxide-based Ion Exchange Membranes (GO IEMs), along with the associated characterization techniques. Secondly, we will present the experimental set-up used for Direct SeaWater Electrolysis (DSWE). This includes a description of the materials used in the various experiments, with a particular emphasis on the electrocatalyst coating methods applied to different porous transport layer materials. We conclude with a discussion of the characterization methods used to evaluate the performance of the DSWE set-ups.

2.1 GO membranes for blue energy applications

2.1.1 GO membrane materials

The materials used for the fabrication of the membranes using dead-end filtration are GO 2% wt, purchased by Graphenea, and Aramid NanoFibers (ANF) in Meta (Nomex) configuration. To create the ANF dispersion 751.23mg of *KOH* are solubilized in a solution containing 250ml DiMethyl SulfOxide (DMSO), together with ethanol drops. Later, 500mg ANF are added to the solution, obtaining a dispersion with 2mg/ml of ANF. For the membrane characterization, potassium chloride *KCl* (0.5M and 1M) and sodium chloride *NaCl* (0.5M) were used. All the chemicals were supplied by Sigma Aldrich.

2.1.2 GO membrane fabrication

Graphene Oxide-based Ion Exchange Membranes (GO IEMs) were fabricated using a dead-end filtration technique (Figure 7). In this method, a liquid solution is placed within a hollow cylinder with a circular porous filter at the bottom. A gas line connected to the top of the cylinder applies pressure to remove the solvent. A circular hydrophilic filter is positioned directly above the porous filter, which retains the solid particles. Due to the presence of a residual solvent inside the final product, after filtration, the membranes were dried on a flat surface at 60 °C under atmospheric pressure, to ensure uniform evaporation of the residual solvent.

The solutions used contained 2 wt% GO in a DiMethyl SulfOxide (DMSO) and water mixture (50:1 weight ratio), along with aramid fibers in the meta configuration at varying concentrations.



Figure 7: Dead-end filtration set-up.

2.1.3 GO membrane characterizations

After the fabrication, the membranes underwent characterization through various techniques. Field Emission Scanning Electron Microscopy (FE-SEM) was employed to assess the thickness and surface properties of the membrane. Subsequently, Fourier Transform Infrared spectrometry (FTIR) was utilized to determine the functional groups of the membranes. Finally, electrochemical measurements were conducted to evaluate the most important properties of these membranes, specifically permselectivity and ionic resistance.

Morphological characterizations

A Field emission scanning electron microscopy analysis was performed to analyze the cross-section of the membranes. FE-SEM is a technology used to analyze the morphology of a specimen under vacuum condition. This microscope uses electrons, generated by a field emission source, to scan the object under study. An electric field gradient accelerates the electrons and optical lenses deflect them. The specimen emits secondary electrons that generate an electrical signal. The advantages of using electrons instead of light are the improved resolution and depth of focus. However, the specimen must be made conductive, so an additional coating layer can be necessary.

Physico-Chemical characterizations

Fourier Transform Infrared Spectroscopy FTIR was used for the physico-chemical analysis. FTIR analysis uses infrared light with variable frequency to scan test samples and observe the intensity of the active vibrational modes of the chemical bonds present in the sample. In the resulting intensity spectrum, two regions can be easily identified: the functional groups region, corresponding to wavenumbers larger than 2000cm^{-1} and the fingerprint region, for wavenumbers smaller than 2000cm^{-1} . The functional group region is used to identify specific chemical bonds, based on their characteristic absorption peaks. In contrast, the fingerprint region is unique to each molecule, providing a complex pattern of peaks.

Electrochemical characterizations

Different electrochemical analyses are pursued on the same membrane to evaluate the permselectivity and ionic resistance of each membrane. These measurements are performed using a side-by-side cell, reported in figure 8. It is composed of two compartments with one inlet and one outlet each, connected to a pump for the flow of the corresponding solution. The membrane is placed between the two compartments, and two gaskets are used at the membrane-cell interfaces to avoid leaking. Two luggin capillaries are integrated to insert the reference electrode inside the compartments, so that they are in contact with the solution. The electrical measurements begin after the two compartments are filled with the corresponding solution.

To calculate the permselectivity, the Open Circuit Potential (OCP) is measured using a side-by-side cell, filled with the same solution on both sides. KCl is typically used for the permselectivity measurements as the mobility of K^+ and Cl^- ions are closer. Permselectivity measurements require a concentration gradient, hence one side of cell is filled with 0.1M KCl and the other one with 0.5M KCl . $Ag/AgCl$ Reference electrodes are used as Sensitive Electrode (SE) and Reference Electrode (RE) (figure 8a). To measure the ionic resistance the side-by-side cell is filled with $NaCl$ at the same concentration, and titanium meshes are used as Working Electrode (WE) and Counter Electrode (CE). In this case, 0.5M $NaCl$ solution is utilized (figure 8b).

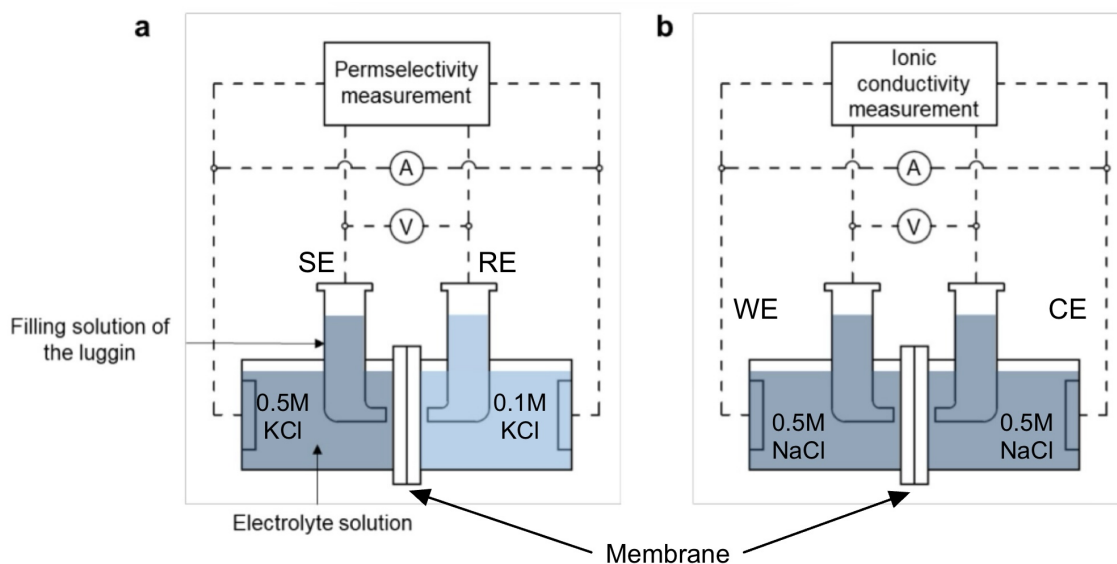


Figure 8: Schematics of the side-by-side cell used for the (a) permselectivity and (b) ionic resistance measurements. Dark blue and light blue represent solutions with different concentrations [25].

Different measurements were carried out: OCP, IV potentiostatic, and VI galvanostatic for the permselectivity and Electrochemical Impedance Spectroscopy (EIS), IV potentiostatic, and VI galvanostatic for the ionic resistance. These experiments are performed three times with a time difference of 30 minutes.

The open circuit measurements consists of an OCP run with a duration of 15 minutes. The IV potentiostatic is a potential sweep from -40mV to 40mV at a scan rate of 0.01V/s . Similarly, the VI galvanostatic is a current sweep from -10mA to 10mA at a scan rate of 0.005A/s . To perform the EIS, used only for the ionic resistance, a frequency ranging from 10^5Hz to 0.1Hz with 5mV amplitude is run. This oscillating potential avoids membrane polarization, while IV potentiostatic and VI galvanostatic shows also effects due to membrane polarization.

The open circuit potential is calculated as the average of the potential values over the 15 minutes run

(figure 3.1). In the case of IV potentiostatic and VI galvanostatic, the OCP potential corresponding to E_{meas} is the potential obtained at a current of 0A, as depicted in figure 9b and 9c, respectively.

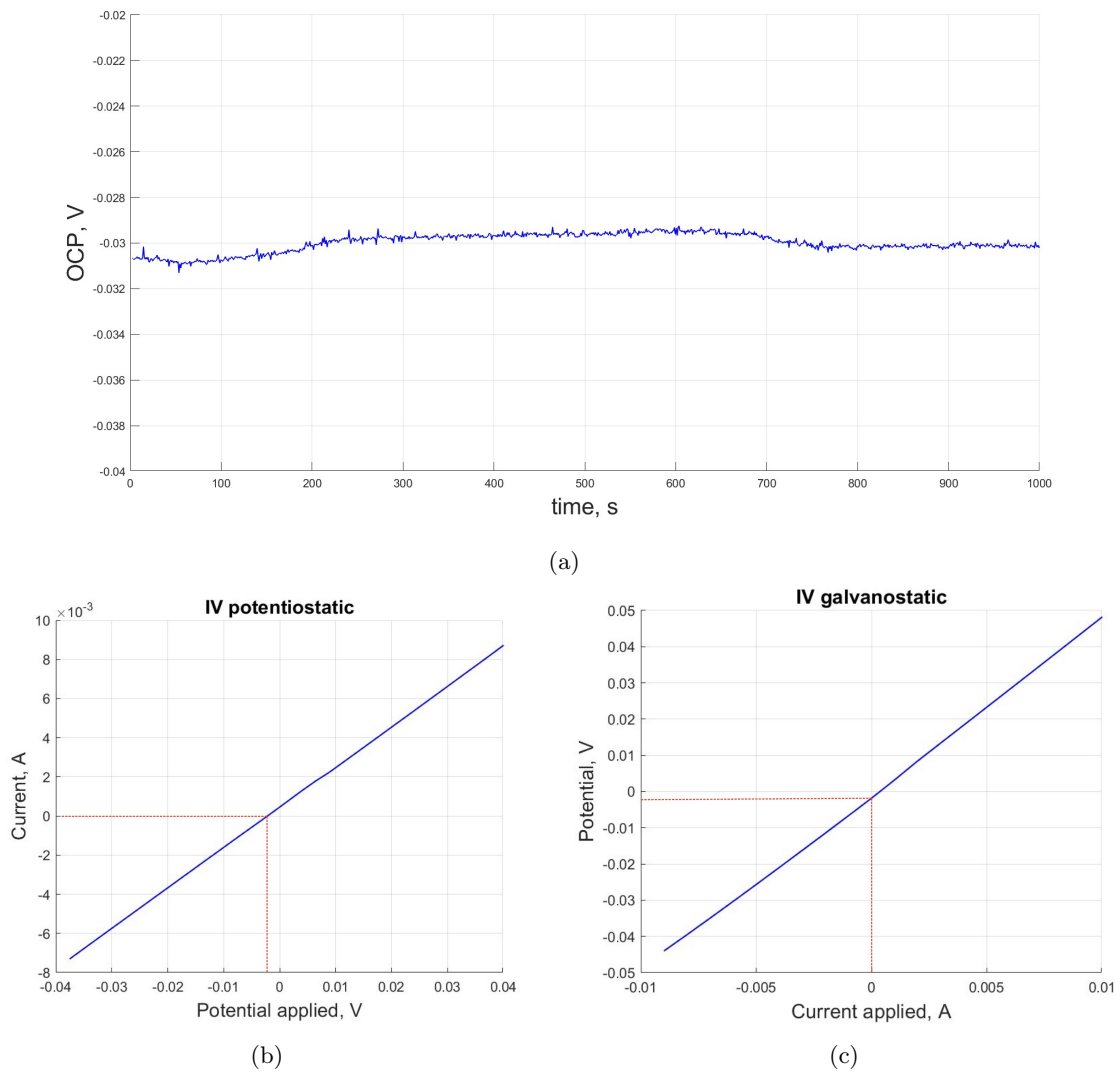


Figure 9: Examples of (a) OCP, (b) IV potentiostatic, and (c) VI galvanostatic measurement to calculate the open circuit voltage.

In the EIS measurement, the ionic resistance corresponds to the real part of the impedance when the imaginary part is 0 in the Nyquist plot, i.e. the plot in which the real part and the negative imaginary part of the impedance are on the x axis and y axis, respectively (figure 10a). In the IV potentiostatic, the resistance is given as the inverse of the slope of the IV curve (figure 10b), while in the VI galvanostatic it corresponds to the slope of the VI curve (figure 10c).

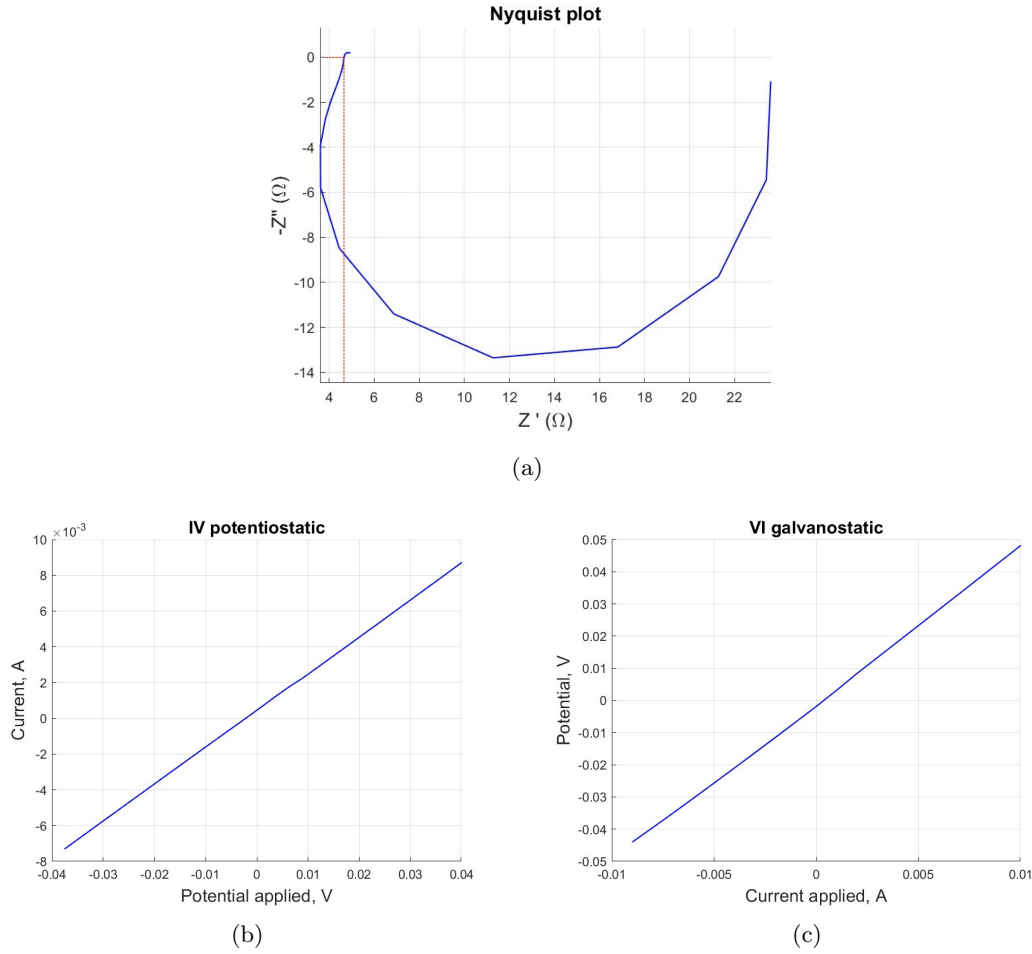


Figure 10: Examples of (a) EIS, (b) IV potentiostatic, and (c) VI galvanostatic measurements to calculate the ionic resistance.

All measurements must also be performed without the membrane, to measure the blank values which must be subtracted from the measured value, isolating the contribute of the membrane only. Blank measurements are performed after the runs.

The apparent permselectivity is calculated as:

$$\alpha_{ap} = \frac{E_{mem}}{E_{the}} \quad (2.1)$$

where E_{the} is the theoretical potential given by the Nernst equation and E_{mem} is the potential across the membrane, given by:

$$E_{mem} = E_{meas} - \Delta E_{offset} - \Delta E_j \quad (2.2)$$

where E_{meas} is the membrane open circuit potential measured using the $Ag/AgCl$ reference electrode, E_{offset} is the difference between the reference electrodes and E_j is the junction potential. The junction potential is the potential difference between the reference electrodes and the electrolyte solution and it is calculated by the Henderson equation, according to the type and concentration of the bulk solution used. In this study, considering the used concentration of the solutions, $E_{the} = -37.02$ mV, $\Delta E_j = -0.80$ mV and ΔE_{offset} is given by the OCP obtained by the blank measurements. In the case of permselectivity measurements, two blanks are necessary because of the different concentration of the solutions. The two blanks will be averaged for the correction.

The ionic resistance is calculated considering the resistance in Ohm multiplied by the active area of the membrane, which is equal to 1.77cm^2 for all membranes. In order to obtain the correct value, the blank resistance must be subtracted considering:

$$R_m = R_{meas} - R_{blank} \quad (2.3)$$

2.2 Bipolar Membranes for DSWE

2.2.1 DSWE system materials

The experimental set-up for direct seawater electrolysis employed the following materials and configurations. A 0.5M solution of sodium chloride ($NaCl$) served as the artificial seawater electrolyte. The anolyte consisted of a 1M sodium hydroxide ($NaOH$) solution, while the catholyte comprised a 1M sodium sulfate (Na_2SO_4) solution. The osmosis cell incorporated a PMG25 polytetrafluoroethylene (PTFE) membrane supplied by POREX Virtek, with a specified thickness of 0.19mm. Reference electrodes for both the cathode and anode were mercury/mercury oxide (Hg/Hg_2O) from Xylem, filled with a 1M potassium hydroxide (KOH) solution. The standard electrode potential of the Hg/Hg_2O half-cell is +0.098V versus the Normal Hydrogen Electrode (NHE) in basic solution. A standard silver/silver chloride ($Ag/AgCl$) reference electrode was also utilized for the cathode.

In all experiments, a symmetric Bipolar Membrane (BPM) from Fumatech (FPM type) was employed, operated at a current density of $1000\text{A}/\text{m}^2$ and maintained at a controlled temperature of $30.0\text{ }^\circ\text{C}$. The Porous Transport Layer (PTL) for the anode and cathode comprised nickel foam (Recemat BV, 1.4mm thick, $440\text{g}/\text{m}^2$ area density), compressed by 25 – 30% to ensure adequate current collector contact. A sintered titanium felt coated with $10\text{g}/\text{m}^2$ platinum-iridium Mixed Metal Oxide (MMO) (total thickness $175\mu\text{m}$, figure 11a), supplied by MAGNETO SPECIAL ANODES, was also utilized. Additional cathode PTL materials included titanium mesh (thickness $150\mu\text{m}$) coated with $60\text{gPt}/\text{m}^2$ (figure 11b), purchased from METAKEM, and sintered nickel felt from Bekaert (1.4mm thickness). Flattened Ti-mesh 2.0 with a $2.5\mu\text{m}$ platinum coating (Metakem) served as the current collector for both the anode and the cathode. A nickel-iron-cobalt ($NiFeCo$) nanopowder from American Elements, with an average particle size range of 80 – 120nm, was used as the HER catalyst. A D2020 Nafion ionomer solution (Ion Power) was employed as a binder on the cathode side. The solutions $NiCl_2$, $FeCl_2$ and $CoCl_2$ used for the electrocatalyst coating on the CEL side are from Sigma-Aldrich. Temperature control was achieved using a Julabo 300F cryostat, and fluid delivery was managed by Masterflex L/S pumps.

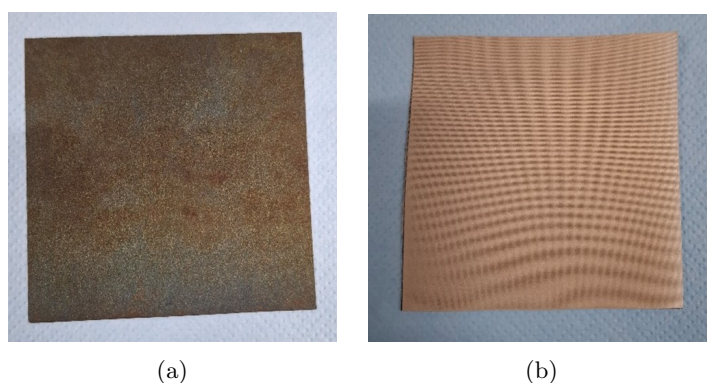


Figure 11: (a) Titanium fiber felt (10cm x 10cm) coated with Ir -MMO ($10\text{g}/\text{m}^2$) for the anode; (b) titanium mesh (10cm x 10cm) coated with Pt ($60\text{g}/\text{m}^2$) for the cathode.

2.2.2 Initial DSWE system

The set-up, shown in figure 12, can be considered as a hybrid system since it comprised an osmotic cell and an electrolyser cell that were connected via the electrolysis cell's catholyte. The osmotic cell, with a flowing rate of 600ml/min, supplied pure water from artificial seawater, made of 0.5M $NaCl$ solution, to the electrolyser via the gas pores of a porous hydrophobic PTFE membrane installed in the osmotic cell designed and made at Wetsus. The anolyte and the catholyte were pumped into the electrolyser cell (100mm x 100mm) through the inlets with a pumping speed, equal to 600ml/min in this work. At the start, 1M sodium sulphate solution was used as the catholyte, providing a conductive environment for ion exchange at the cathode. The anolyte, which served as the source of hydroxide ions for the anode reaction of the bipolar membrane electrolyser, was made of 1M $NaOH$ solution. The electrolyser cell comprised a bipolar membrane BPM with one manifold inlet and one manifold outlet for the anolyte and the catholyte. The catholyte and the anolyte were stored in two separated PVC tanks for safety, as well as the (artificial) seawater. Each tank had inlets and outlets used for pumping out the solution and for pumping in.

The set-up was kept in isothermal conditions at 30.0 °C by means of a cryostat and by using three flat plate heat exchangers. This temperature is dictated by the specifications of the commercial BPM used. In the system, also an external thermocouple (Pt-100 sensor) is used for the cryostat to detect the actual temperature of the catholyte before it enters the electrolyser cell. A cryostat is preferred to a thermostat since it can also be used to lower the temperature, which can increase due to the Ohmic losses inside the electrolyser cell.

The hydrogen and oxygen produced must be well separated and disposed of via the fume hood. A Draeger hydrogen gas detector is installed in the set-up to detect any possible hydrogen leaks. If the detector senses hydrogen levels reaching 400 ppm in the fume hood, it will immediately cut off the current. This is crucial because the energy required to ignite hydrogen gas is only 0.02 millijoules.

Initially, two different types of reference electrodes were used: one for the anode potential (reference electrode is Hg/HgO (1M KOH)) and one for the cathode potential (reference electrode is $Ag/AgCl$). However, the $Ag/AgCl$ reference electrode for the cathode was replaced by Hg/HgO (1M KOH) reference electrode for the direct measurement of the bipolar membrane voltage at $1000A/m^2$ during electrolysis. The reference electrode must adhere to the following conditions: firstly, it must maintain a stable potential. Secondly, it should be reversible, meaning it must facilitate rapid reactions at the electrodes, with permissible low currents only in the range of pA to fA. Lastly, it is essential here that no chloride (Cl^-), bromide (Br^-), or iodide (I^-) ions are present in the reference electrode. For this reason, the standard $Ag/AgCl$ reference electrode was substituted by the Hg/HgO reference electrode, which does not contain any chloride, bromide or iodide.

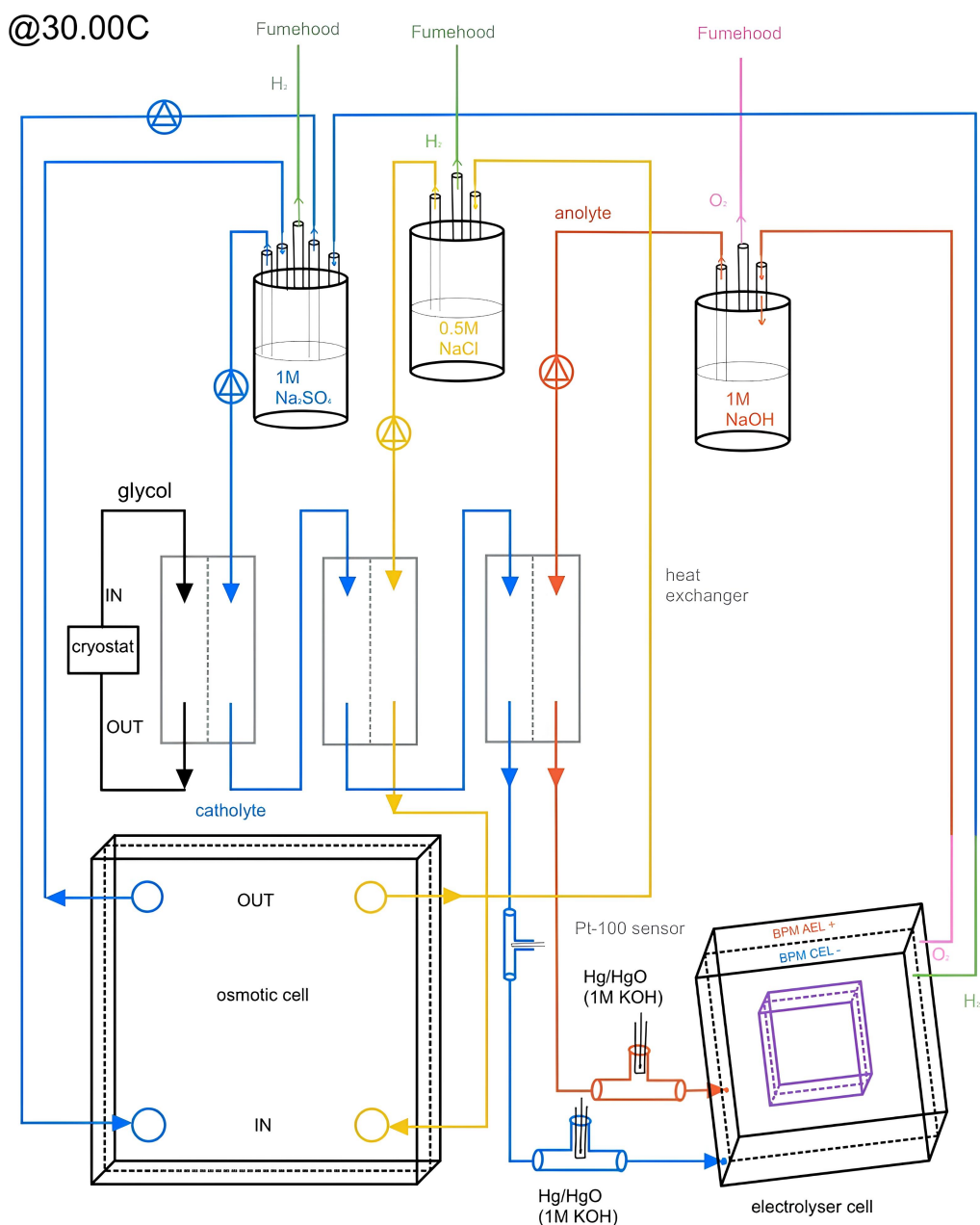


Figure 12: Schematics of the hybrid set-up for direct seawater electrolysis using a bipolar membrane electrolysis cell combined with an osmosis cell to extract pure water from 0.5M NaCl used as artificial seawater. Blue lines correspond to the catholyte (Na_2SO_4), yellow lines to the artificial seawater (NaCl), and red lines to the anolyte (NaOH). Green and pink lines represent the hydrogen and oxygen gases generated.

Figure 13 reports a visual representation of the experimental set-up for seawater electrolysis. The image showcases several key components of the system: the Julabo cryostat for thermostating the set-up at 30 °C and the attached Masterflex pumps for anolyte and artificial seawater circulation (right side), the electrolyser cell (left side) sealed with blue gaskets and connected to separate cylindrical electrolyte reservoirs for anolyte and catholyte. Three heat exchangers are located behind the electrolyser cell, while the catholyte pump and seawater storage tank with 10L 0.5M NaCl are visible in the background.

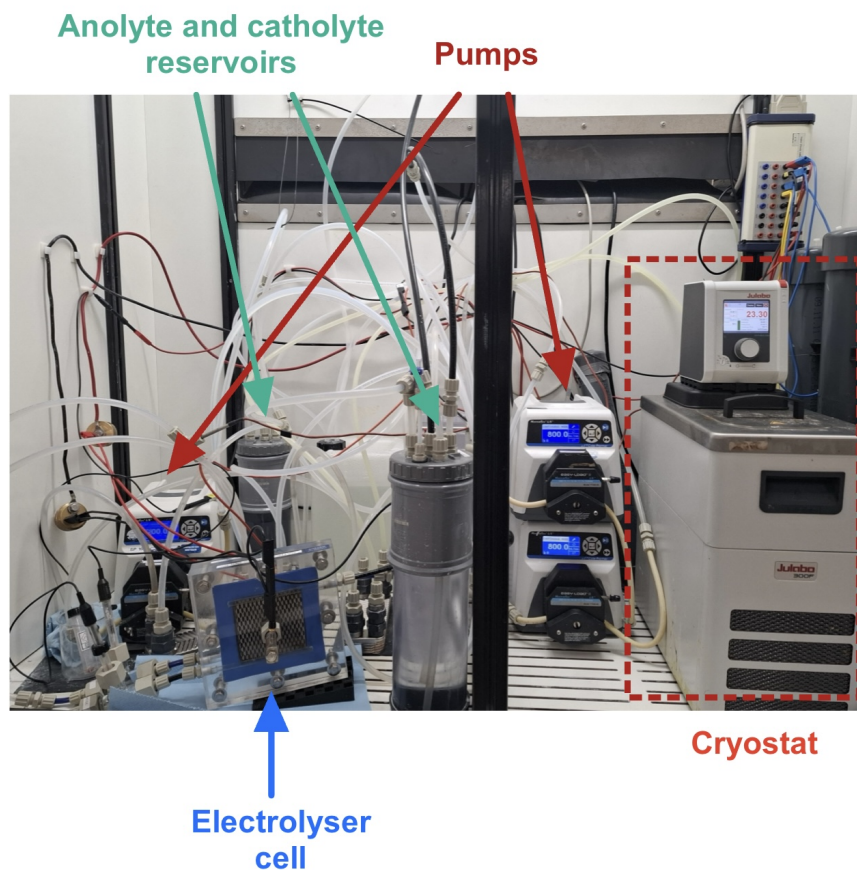


Figure 13: Hybrid set-up for direct seawater electrolysis using a bipolar membrane electrolysis cell combined with an osmosis cell to extract pure water from 0.5M $NaCl$ as artificial seawater.

This thesis focuses on the optimization of the bipolar membrane electrolyser cell, particularly on the application of the catalyst for the HER and OER processes at the cathode and anode side, respectively. Figure 14 reports a schematic of the electrolyser cell used in this study. The most important part is the separator, in our case the symmetric commercial bipolar membrane from Fumatech. For water electrolysis, the bipolar membrane was used in reverse mode condition, meaning that on the AEL side there is the anode, while on the CEL side there is the cathode. A Porous Transport Layer (PTL) was used to contact the BPM with the electrocatalyst. The electrocatalyst can not be directly coated as the bipolar membrane is offered by Fumatech in a wet condition. Finally, platinized titanium current collectors were used on both sides of the electrolyser cell. The electrolyser cell used in this study was a 10cm x 10cm cell that was sealed using fluorinated silicone-type gaskets.

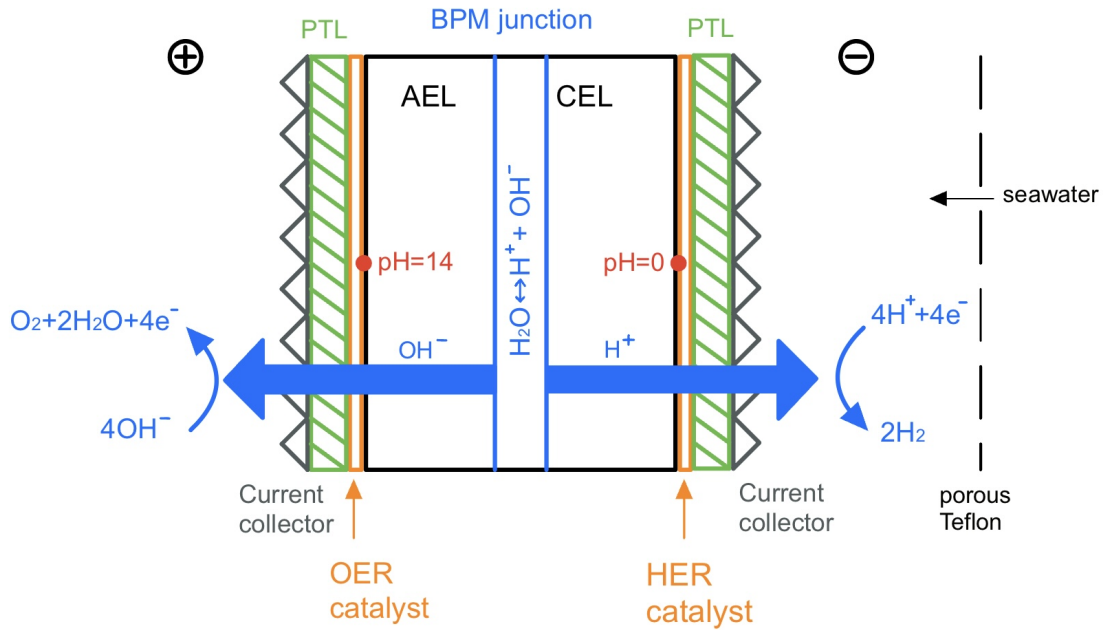


Figure 14: Schematics of the configuration of the bipolar membrane electrolyser cell. The HER and OER catalysts are represented by the orange layers, while the Porous Transport Layers (PTLs) correspond to the green regions. At the AEL/CEL interface there is the BPM junction, depicted in blue, where the water splitting reaction occurs. The current collectors at the anode and cathode side are reported in gray. The porous Teflon membrane of the osmosis cell is reported on the cathode side.

Figure 15 shows the sealed electrolyser cell from the anode side and from the cathode side. Note the difference in color due to the use of titanium fiber felt coated with $10\text{g}/\text{m}^2$ $\text{Pt} - \text{Ir}$ -MMO for the anode (figure 15a) and a thin titanium mesh coated with $60\text{g}/\text{m}^2$ of platinum for the cathode (figure 15b).

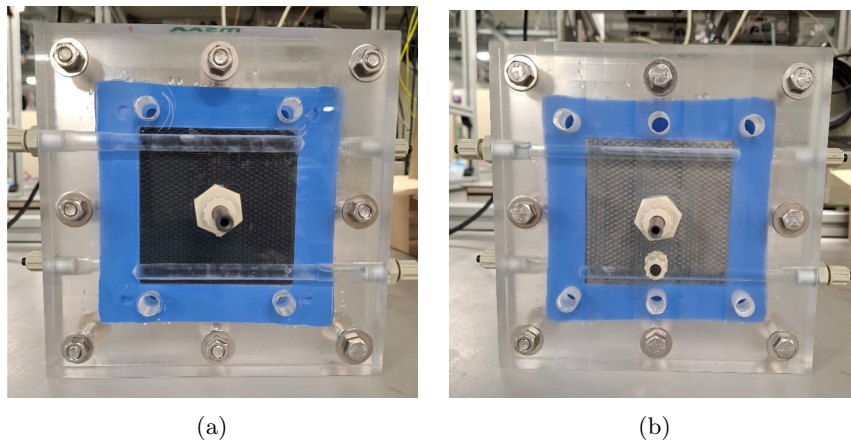


Figure 15: Electrolyser cell (10cm x 10cm): (a) Anode side; (b) Cathode side.

Note that in this electrolyser cell configuration the seawater is contacted with the catholyte of the electrolyser cell via a porous Teflon membrane with the 0.5M NaCl solution of the osmosis cell.

First test

The initial bipolar membrane electrolysis test utilized Ni -foam without electrocatalyst coated as both

anode and cathode, compressed 25-30% for current collector contact. This pressure contact is useful to create a very low ohmic electrical contact between the nickel foam and the metal current collector. The cathode current collector was a flattened *Ti*-mesh 2.0 with $2.5\mu\text{m}$ platinum coating, while the anode used titanium fiber felt coated with $10\text{g}/\text{m}^2$ platinum-iridium mixed metal oxide. No electrocatalysts were applied to the *Ni*-foam electrodes used for the cathode side.

Second test

The materials for the second test included five layers of $10\text{g}/\text{m}^2$ platinum-iridium mixed metal oxide coated sintered titanium felt (total thickness $175\mu\text{m}$, (figure 11a)) as anode, with a platinum-iridium coated *Ti*-mesh as current collector. As cathode, five layers of very thin titanium mesh (thickness $150\mu\text{m}$) coated with $60\text{g}/\text{m}^2$ (figure 11b), were used. The cathode used a *Ti*-mesh 1.0 coated with platinum as current collector.

Third test

Lastly, a *Hg/HgO* reference electrode was included with a 1M *KOH* filling solution. From this moment on the anode remained five layers of platinum-iridium oxide coated sintered titanium felt contacted with a platinum-iridium coated *Ti*-mesh as current collector, since stable results were obtained for the anode potential at $1000\text{A}/\text{m}^2$. Thus, we will focus on the optimization of the cathode side, specifically, on the electrocatalyst material and coating techniques.

Fourth test

For electrically contacting the anode and cathode, two layers of *Ni*-foam ($440\text{g}/\text{m}^2$) with 1.4mm thickness each were added. For the cathode, the PTL was composed of two layers of nickel foam, each 1.4mm thick, combined with five layers of $60\text{g}/\text{m}^2$ platinum-coated sintered titanium felt to facilitate effective ion transport and reaction kinetics.

Fifth test

In the fifth test the five platinum coated *Ti*-mesh layers of $150\mu\text{m}$ at the cathode were replaced with two layers of *Ni*-foam of 1.4mm and one layer of *Ni*-foam of 0.30mm.

Subsequent Tests

In later experiments, one of the *Ni*-foam layers of the previous test was substituted by a porous nickel substrate (sintered *Ni*-felt or *Ni*-foam) that was coated before assembly of the electrolysis cell with a HER catalyst using different coating methods and catalyst dispersion composition. Firstly, a *NiFeCo* nanopowder was used as an HER catalyst, including the use of Nafion ionomer solution as binding agent. Later, dip-coating was employed for both sintered nickel felt and nickel foam using a different dispersion for the coating of a *NiFeCo*-based HER catalyst at the cathode side.

Electrocatalyst coating methods

Ultraturrax-assisted coating

For electrocatalyst coating on the cathode side, a catalytic ink was prepared using 25mL of a 20 wt% Nafion solution and 25g of iron-nickel-cobalt (*NiFeCo*) alloy nanopowder. The solution, with a 5g Nafion content, was sonicated using an Ultraturrax stirrer at 20000rpm. To this, 475mL of a solution containing 2-propanol and water (1:3 v/v) was added, resulting in a final composition of 83.3 wt% *NiFeCo* and 16.6 wt% Nafion binder in water. This ratio is important to ensure adequate solution homogeneity while maintaining a sufficient proportion of the electrocatalyst to achieve an effective catalytic activity.

A cooling system, employing an ice bath (figure 16), was implemented to dissipate heat generated during the Ultraturrax mixing process. To further stabilize the dispersion, 144mg of sodium dodecyl

sulfate (*SDS*, 288mg/mol) was added.

The sintered *Ni*-felt was selected as a substrate for the catalytic coating since many studies suggest that it shows the best catalytic HER activity [26] thanks to its high corrosion resistance in alkaline environments and its non-noble metal nature. Moreover, this substrate is hydrophilic and has high electrical conductivity and porosity.

Prior to coating, the nickel felt substrate was washed with 2-propanol to remove surface contaminants and ensure proper adhesion of the coating. The cleaned *Ni*-felt was then dipped into the catalytic dispersion for a few seconds to deposit the catalyst layer.

The 1.4mm sintered nickel felt coated with *NiFeCo*, together with a nickel foam layer of 1.4mm and a nickel foam layer of 0.3mm, was used as the cathode side for the electrolyser cell.



Figure 16: System used for the Ultraturrax-assisted coating of sintered nickel felt with *NiFeCo* electrocatalyst, showing the Ultraturrax at 20000rpm and the integrated ice bath.

Vacuum-assisted infiltration coating

To improve catalyst distribution throughout the high-density *Ni*-felt, a vacuum-assisted coating method was developed. This new developed system incorporates a vacuum pump to generate a pressure difference, facilitating the transport of the nanopowder particles through the entire cross-section of the substrate.

In this procedure, a circular sintered nickel felt is placed on a filter paper within a porous circular ceramic support, called Buchner funnel. The Buchner funnel is then positioned inside a vacuum connected Erlenmeyer of glass, using rubber gaskets for sealing the Buchner funnel, connected to a vacuum pump. The catalytic dispersion was composed of 5g Nafion, 25g nanoparticles of *NiFeCo*, 475mL of 2-propanol and water (1:3 v/v) and 144mg of *SDS*. As in the previous method, the mixture was poured onto the *Ni*-felt surface, and the vacuum pump was activated. Due to the presence of Co nanoparticles in the nanopowder, this process must be done in the fume-hood.

As shown in figure 17, the pressure difference made the dispersion go through the entire thickness of the *Ni*-felt substrate, evidenced by the black-colored dispersion filling the bottom part of the vacuum

Erlenmeyer. After air-drying overnight, the coated nickel felt was employed as the porous transport layer at the cathode side of the bipolar membrane electrolyser cell. The coated side was oriented toward the bipolar membrane, where the hydrogen evolution reaction occurred.



Figure 17: System used for the vacuum-assisted coating of $NiFeCo$ on the sintered nickel felt substrate, showing the vacuum pump and the Buchner funnel containing the filter.

Dip-coating

The issues related to the previous coated substrate are related to the use of the HER catalyst in the form of nanopowder, composed by high density particles with a very small diameters that made it very difficult to create a homogeneous dispersion. This led to the formation of precipitates at the bottom of the bottle containing the nanoparticle solution, and additional stirring using the Ultraturrax mixer solved this settling issue only temporarily. That is why a completely different coating technique was used, avoiding the use of the $NiFeCo$ nanopowder.

The dense sintered nickel felt surface was etched with a 1M HCl solution for 30 minutes, to remove NiO layer from the nickel surface. After that, the nickel felt was horizontally placed in a glass container for two weeks in solution containing 23.8g/L $NiCl_2$, 2.0g/L $FeCl_2$, and 29.98g/L $CoCl_2$. The container was taped with Parafilm to avoid the evaporation of the solution.

Another option is to use a nickel foam placed vertically in a plastic container. The container was again sealed using Parafilm.

2.2.3 DSWE characterizations

Morphological characterizations

A Scanning Electron Microscopy (SEM) analysis was performed to analyze the structure of the PTL coated with the catalyst for the HER process. SEM is a technology used to analyze the topography of a specimen under vacuum condition. This microscope uses electrons, generated by a field emission source, to scan the object under study. An electric field gradient accelerates the electrons and optical lenses deflect them. The specimen emits secondary electrons that generate an electrical signal. The advantages of using electrons instead of light are the improved resolution and depth of focus. However, the specimen must be made conductive, but in our case no additional coating layer is necessary, since all the substrates used were Ni-based.

Chemical characterizations

Energy Dispersive X-Ray spectroscopy (EDX) is a chemical analysis capable of identifying the elements present in the sample under study, as well as their amount. A beam of X-rays is focused on the sample exciting electrons in the inner shell of the atoms in the sample. The so-created hole is then filled by an electron coming from a shell with higher energy. The difference between these energies is then emitted in the form of an X-ray. In this way, a particular electromagnetic spectrum is obtained, with peaks that depend on the atomic structure of the sample. This chemical analysis allows the estimation of the concentration of each element in the sample.

Electrochemical characterizations

Electrochemical analysis was conducted to evaluate four potentials: cell potential, anode and cathode potentials, and BPM potential. This electrochemical analysis was performed using IVIUM software and a potentiostat while the direct current of 10A was supplied by power supply from DELTA ELEKTRONIKA. Chronopotentiometry was carried out with a current range of 100nA (the potentiostat is not generating the DC current for electrolysis, this was done by the external power source) and a potential range of 10V, with a sampling rate of one second. The analysis was run every test for four hours to assess cell stability over time. Before initiating the electrical analysis, the pumps and cryostat were activated. Once the cryostat stabilized the temperature at 30.0°C, the DELTA ELEKTRONIKA power source applied the $1000A/m^2$ current density, and IVIUM software started data recording. After the four-hour run, the current was stopped automatically, and the data were extracted from the IVIUM software. This process was repeated four times per test, though some measurements were shorter due to some IVIUM software issues.

In this study, the set-up operated at a current density of $1000A/m^2$, with a total current applied of 10A, a limit imposed by the commercial bipolar membrane used (Fumatech FPM). Exceeding this current density could lead to membrane dehydration due to excessive water consumption, ultimately causing membrane failure, as the manufacturer specifies that the membrane must remain hydrated. The voltage efficiency VE is defined as:

$$VE = \frac{E_{minimum}}{E_{cell}} \times 100\% \quad (2.4)$$

where $E_{minimum}$ is the minimum voltage necessary for the water electrolysis, equal to 1.229V and E_{cell} is the actual cell potential at a given current density of, for instance, $1000A/m^2$. However, this definition is only valid for conventional electrolysis cells like the Proton Exchange Membrane Electrolysis cell and the Alkaline Water Electrolysis cell. In the case of the Bipolar Membrane Electrolysis cell, the measured cell voltage minus the bipolar membrane voltage (E_{BPM}) can be compared to the conventional cell voltage E_{cell} . In the case of bipolar membrane electrolysis, the cell voltage at a given current density is built up from four components:

- The anode potential as measured vs a reference electrode;
- The cathode potential as measured vs a reference electrode;
- The bipolar membrane voltage as the voltage measured between two reference electrodes;
- The ohmic voltage loss inside the Bipolar Membrane Electrolysis cell.

Therefore, the voltage efficiency for the electrode reactions of BPM electrolysis can be calculated via an alternative definition as:

$$VE = \frac{E_{minimum}}{E_{cell} - E_{BPM}} \times 100\% \quad (2.5)$$

To evaluate the efficiency of the water electrolysis systems, the anode and cathode overpotentials are important values that must be determined. The overpotential is the extra voltage required to drive an electrochemical reaction at a given current density. Ideally, a reaction with zero activation energy would occur exactly at its standard potential, however, electrochemical reactions require an activation energy that is represented by the overpotentials. The anode and cathode overpotential, given in Volt, are defined as:

$$\eta_{anode} = E_{anode} - E_{(OH^-, O_2)}^0 \quad (2.6)$$

$$\eta_{cathode} = E_{cathode} - E_{(H^+, H_2)}^0 \quad (2.7)$$

where anodically the following reaction is assumed vs NHE



and cathodically we assume proton reduction, according to the following reaction vs NHE



with E_{anode} and $E_{cathode}$ being the measured anode and cathode potential vs NHE. In our case, two identical reference electrodes Hg/HgO (1M KOH) were used, with the standard electrode potential of the Mercury/Mercury Oxide (1M KOH) reference electrode is equal to +0.098V vs NHE. The potential difference between both Hg/HgO (1M KOH) reference electrodes was identical to the bipolar membrane voltage at the given current density in our set-up.

Results and Discussion

In this chapter, the results of the GO membrane fabrication and characterization are presented. Later, the outcomes of the morphological, chemical, and electrical analysis of the DSWE systems are discussed.

3.1 GO membranes for blue energy applications

3.1.1 GO membranes fabrication

In this study, four distinct combinations of Graphene Oxide (GO) content and Aramid NanoFiber (ANF) concentrations were examined: 10 mg and 15 mg of GO, each paired with 25% and 50% ANF. The dead-end filtration process was conducted at varying pressures ranging from 5 to 8 bar, resulting in different filtration and drying times. The fabrication parameters and the corresponding filtration and drying times for the membranes containing 10 mg GO are reported in table 2 as example. As expected, higher applied pressures resulted in faster filtration times. Additionally, the drying time appeared to be independent of the applied pressure and remained relatively constant for all the cases. As illustrated in figure 18, all the fabricated membranes share a diameter of 4.7 cm, determined by the size hollow cylinder employed in the process.

Figure 18b shows that the fabricated membranes exhibit different surface roughness. This variation can be attributed to the applied pressure during the fabrication process, which influence the filtration time.

Table 2: Fabrication parameters and corresponding filtration and drying time for the membranes containing 10 mg of graphene oxide and a differen ANF content.

Type of membrane	Pressure	Filtration time	Drying time @60C
10 mg GO, 25% ANF	5 bar	90 min	30 min
	7.5 bar	30 min	30 min
10 mg GO, 50% ANF	5 bar	60 min	45 min
	7.5 bar	45 min	30 min

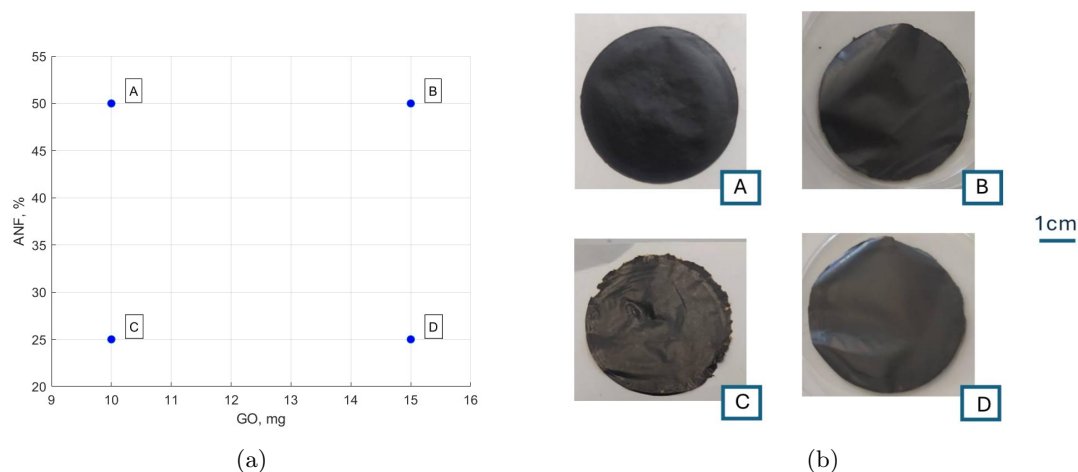


Figure 18: Fabricated membranes: (a) used concentrations of GO and ANF; (b) photos of the membranes after the drying.

3.1.2 GO membrane characterizations

Morphological characterizations

From the SEM analysis in figure 19, the thickness of the membranes was determined to range between $3 - 8\mu\text{m}$. Additionally, figure 19c reveals the formation of aramid nanofiber clusters of different sizes within the membrane. These clusters arise from the aggregation of ANFs during the fabrication process, which can influence the mechanical properties and uniformity of the membrane. This outcome highlights the need for optimization in the dispersion of the nanofibers to ensure consistent performance across the membrane.

SEM analysis was performed on the membranes before and after the electrochemical characterizations. The thickness of the membrane after the OCP measurement increases, as the water causes the membrane to swell. This phenomenon is a direct consequence of the hydrophilic nature of the materials, which absorb water and cause the expansion of the membrane.

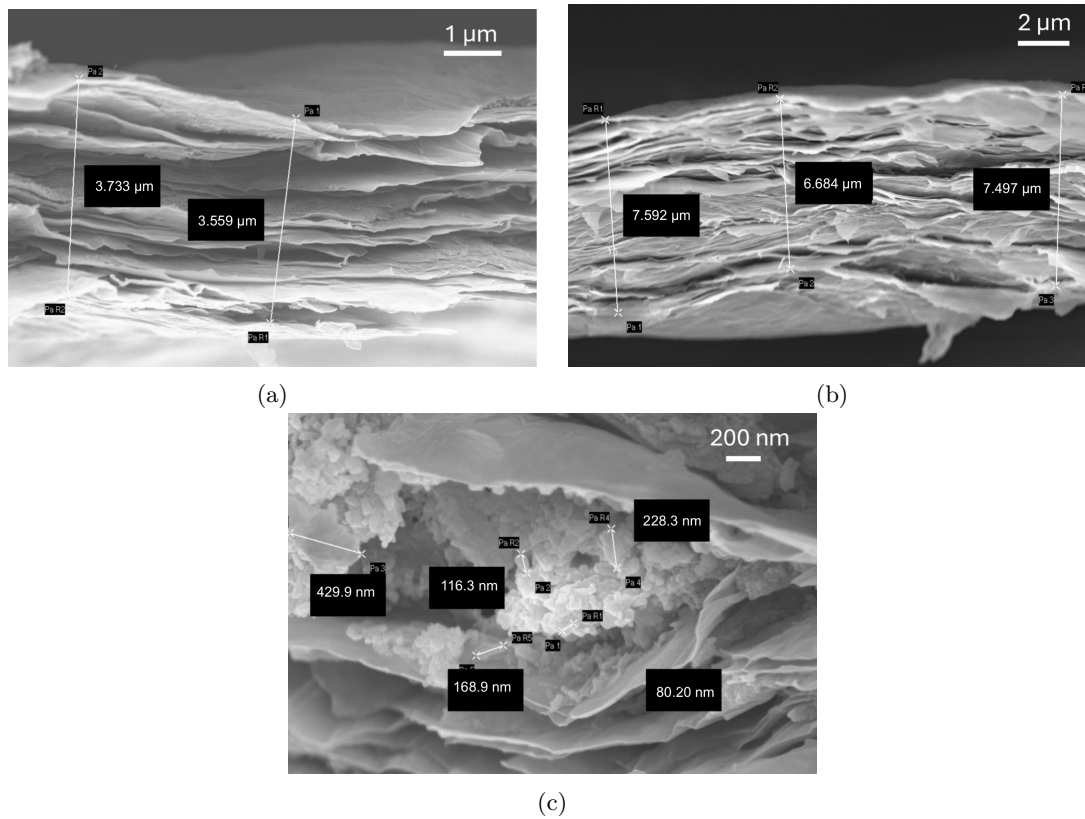


Figure 19: FESEM analysis of different membranes. (a) 10mg GO with 25% ANF; (b) 10mg GO with 25% ANF after the OCP measurement; (c) 10mg GO with 50% ANF.

Physico-Chemical characterizations

FTIR analysis was conducted on the graphene oxide membrane, on the aramid nanofibers alone, and on the composite membrane fabricated with both GO and ANF to identify the individual contributions of each component and their combined effect in the composite membrane. Figure 20 reports, as example, the FTIR spectrum of the membrane composed by 15mg GO and 50% ANF. Because of the different functional groups, the three samples have different spectrum. Graphene oxide's spectrum (in blue in figure 20) has three main peaks at 3200cm^{-1} , 1600cm^{-1} and 1050cm^{-1} , corresponding to the OH , $C-O$ and $C=O$ bonds, respectively. Instead, the ANF spectrum (in red in figure 20) has a peak corresponding to the triple bond $C\equiv O$, at 2400cm^{-1} . As predicted, the spectrum of the composite membrane is a combination of the individual spectra of GO and ANF, indicating that the chemical structures of both components are preserved within the composite membrane. For example, the $C-O$ single bond peak around 1050cm^{-1} , which is characteristic of GO, and the triple bond peak near 2400cm^{-1} , typical of ANF, are present also in the membrane spectrum.

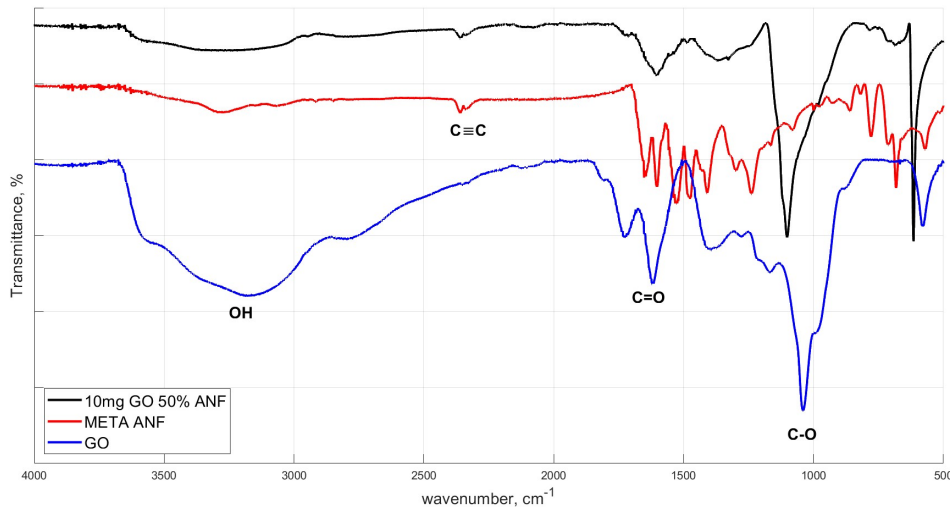


Figure 20: FTIR spectra of GO (blue), aramid fibers (red) and of the membrane containing 15mg GO and 25% ANF (black).

Electrochemical characterizations

The electrochemical performance of the GO-IEMs, as characterized by Open Circuit Potential (OCP) and ionic resistance measurements, reveals insights into the membrane's ion selectivity and conductivity.

The figure 21 shows the OCP values calculated using an OCP measurements with a duration of 15 minutes for the four composite membranes. The two blank measurements at 0.1M and 0.5M *NaCl* have been subtracted from the measured values as:

$$OCP_{membrane} = OCP_{measured} - \left(\frac{OCP_{blank0.1M} + OCP_{blank0.5M}}{2} \right) \quad (3.1)$$

Table 3 reports the measured open circuit voltages as well as the two blank measurements at 0.1M and 0.5M *NaCl* for the four membranes. The membrane open circuit voltage is calculated according to equation (3.1).

Table 3: Open circuit voltages values for the four membranes calculated as an average of a 15 minutes OCP measurements. Two blank measurements are necessary because two solutions are used. The OCP membrane is calculated as equation (3.1).

Type of membrane	OCP measured	OCP blank 0.1M	OCP blank 0.5M	OCP Membrane
10 mg GO, 25% ANF	32.16 mV	2.32 mV	2.14 mV	30.22 mV
10 mg GO, 50% ANF	32.45 mV	2.47 mV	1.95 mV	30.25 mV
15 mg GO, 25% ANF	34.70 mV	2.58 mV	1.24 mV	32.78 mV
15 mg GO, 50% ANF	33.96 mV	3.41 mV	1.90 mV	31.31 mV

As seen in figure 21, the OCP values appear relatively stable across varying aramid nanofiber percentages, particularly at a 10mg GO. Specifically, the OCP values hover around 30mV for both 25% and 50% ANF concentrations. At a higher GO weight of 15mg, a slight divergence emerges, with the 25% ANF sample exhibiting a higher OCP (approximately 32.7mV) compared to the 50% ANF sample (around 31.3mV). This suggests that increasing the GO loading and reducing the ANF content may enhance the membrane's ability to selectively transport ions.

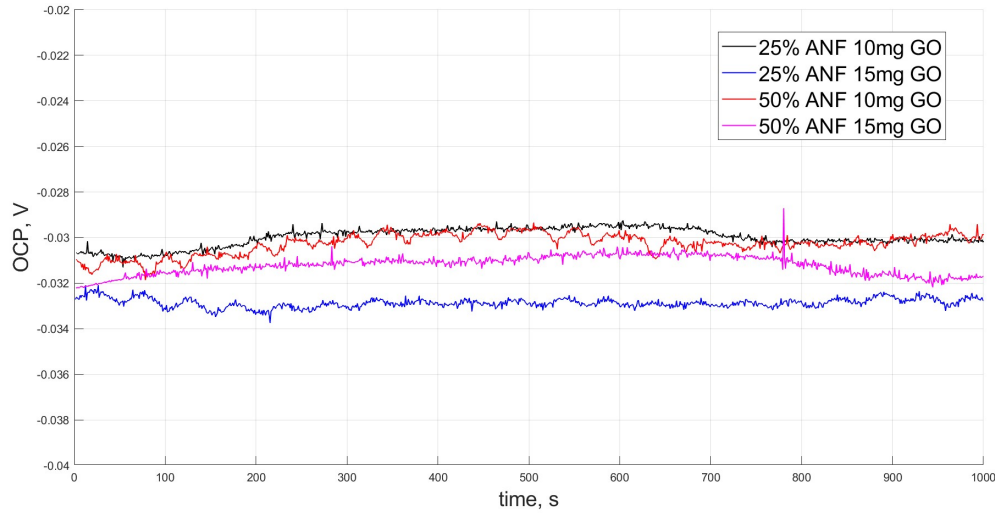


Figure 21: Open circuit voltage evolution over time for the four composite membranes. All the values have been corrected with the corresponding blank measurements.

The permselectivity was calculated from the OCP, without considering the ion transport number, dividing the membrane potential by the theoretical potential calculated by the Nerst equation, as in the equation (2.1).

The ionic resistance measured values for the four membranes derived from EIS, IV potentiostatic, and VI galvanostatic measurements are reported in the table 4. All the values have been corrected with the corresponding blank measurements, according to equation (2.3). Figure 22 shows an example of the IV potentiostatic and VI galvanostatic measurements results of the membranes with 10mg GO and different ANF content. The difference in the slope of the two curves represent the different ionic resistance of the two membranes. Figure 23b illustrates a more pronounced dependence of ionic resistance on both GO loading and ANF percentage. At 10 mg of GO, the ionic resistance is relatively low (approximately $1.7 \Omega \cdot cm^2$) for the 50% ANF sample, increasing to $3.2 \Omega \cdot cm^2$ for the 25% ANF sample. However, at 15mg GO weight, the ionic resistance increases significantly, reaching $2.7 \Omega \cdot cm^2$ for the 25% ANF sample and $4 \Omega \cdot cm^2$ for the 50% ANF sample. This trend suggests that increasing both GO loading and ANF content do not provide the same result. In particular, at 10mg GO, increasing the ANF concentration reduces the ionic resistance (figure 22), while at 15mg GO, the ionic resistance is lower for the 25% content of ANF.

While increasing GO loading may initially enhance permselectivity, it can also lead to increased ionic resistance, particularly at higher ANF concentrations. The summary of these results are reported in table 5.

Table 4: Ionic resistance measured values for the four membranes derived from EIS, IV potentiostatic, and VI galvanostatic measurements. All the values have been corrected with the corresponding blank measurements.

Type of membrane	IONIC RESISTANCE (IV)	IONIC RESISTANCE (VI)	IONIC RESISTANCE (EIS)
10 mg GO, 25% ANF	$3.22 \Omega \cdot cm^2$	$3.10 \Omega \cdot cm^2$	$3.20 \Omega \cdot cm^2$
10 mg GO, 50% ANF	$1.78 \Omega \cdot cm^2$	$1.85 \Omega \cdot cm^2$	$1.54 \Omega \cdot cm^2$
15 mg GO, 25% ANF	$2.80 \Omega \cdot cm^2$	$2.70 \Omega \cdot cm^2$	$2.59 \Omega \cdot cm^2$
15 mg GO, 50% ANF	$4.11 \Omega \cdot cm^2$	$4.11 \Omega \cdot cm^2$	$3.76 \Omega \cdot cm^2$

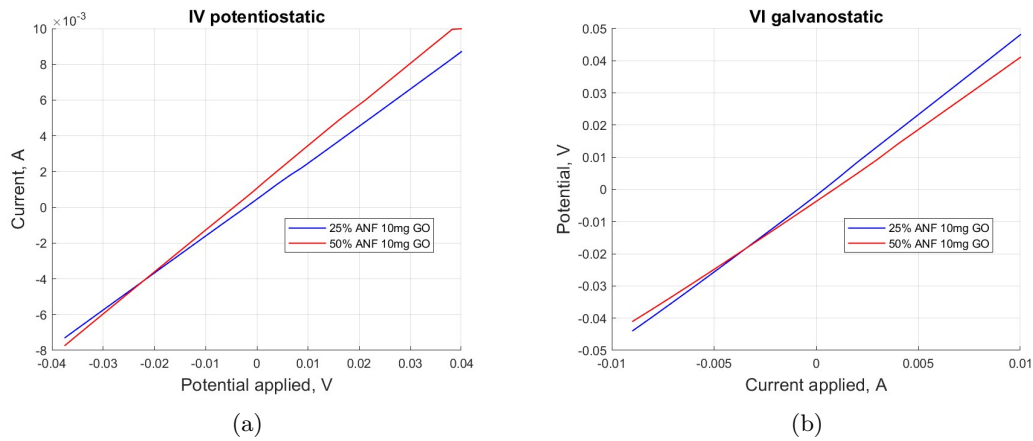
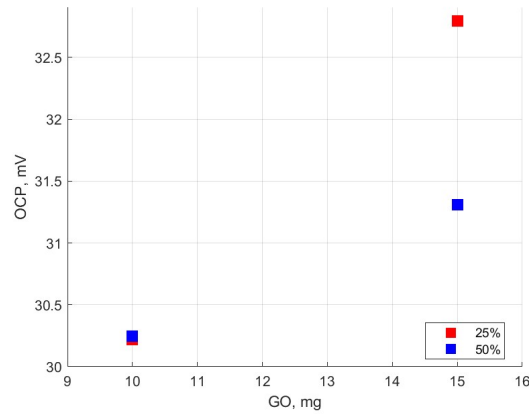


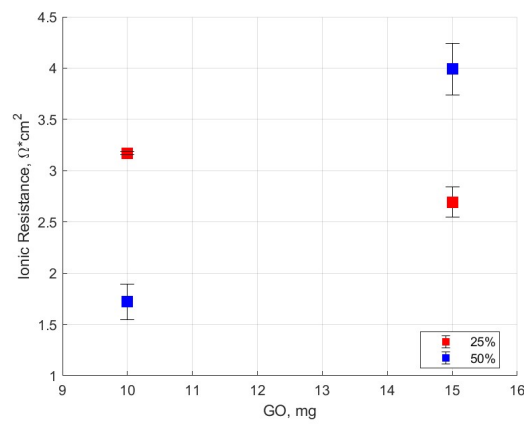
Figure 22: (a) Potentiostatic current-voltage (IV) and (b) galvanostatic voltage-current (VI) analyses of composite membranes with varying aramid nanofibers concentrations. Increasing ANF content while maintaining constant GO mass resulted in increased ionic resistance. This trend is demonstrated by a steeper linear regression slope in the IV curve and a reduced slope in the VI curve.

Table 5: Open circuit voltage, permselectivity and ionic resistance measured values for the four membranes. Ionic resistance is calculated as the average of values derived from EIS, IV potentiostatic, and VI galvanostatic measurements. All the values have been corrected with the corresponding blank measurements.

Type of membrane	OCP, mV	PERMSELECTIVITY	IONIC RESISTANCE, $\Omega \cdot cm^2$
10 mg GO, 25% ANF	30.2	83.8%	3.2 ± 0.02
10 mg GO, 50% ANF	30.3	83.9%	1.7 ± 0.2
15 mg GO, 25% ANF	32.8	90.7%	2.7 ± 0.2
15 mg GO, 50% ANF	31.3	86.7%	4.0 ± 0.3



(a)



(b)

Figure 23: (a) OCP and (b) ionic resistance values the four membranes. Error bars correspond to the standard deviation of each value. All the values have been corrected with the corresponding blank measurements.

The ionic resistance value is lower than those reported in similar work in GO-based membrane [27]. However, the permselectivity achieved with these GO-based membranes are still worse than the one obtained in other similar studies.

3.1.3 Scaling up trial

Graphene Oxide (GO) membranes show promise as sustainable alternatives to polymeric membranes, but scaling up their fabrication for industrial applications remains challenging. The dead-end filtration method used in the study produces membranes limited to a 4.7cm diameter due to the fixed diameter of the porous filter and the hollow cylinder, which highlights a critical barrier for industrial applications. In order to overcome this scaling up issue, the Roll-to-Roll (R2R) process offers a viable alternative for large-area graphene oxide membrane production. This method (figure 24) employs a continuous coating technique where slurries are deposited onto thin, flexible substrates threaded through a series of rollers [28].

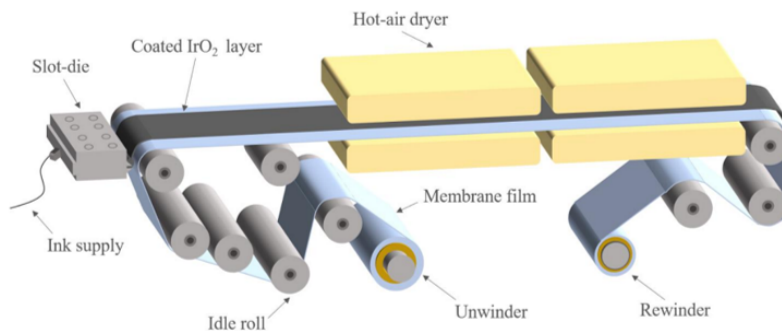


Figure 24: Schematics of the roll-to-roll process [29].

The material that must be coated, in our case GO, is poured on the flexible substrate and passed through the rolls. The membrane is then dried in an oven and possess tunable thickness and theoretically limitless length. However, a critical challenge of this technique is related to the low GO viscosity, being GO 2% wt, the only commercial available concentration. This concentration is not high enough to avoid splashing during the R2R process.

To address this issue, GO concentration was enhanced via centrifugation. The 2% GO was centrifugated using different velocities and at different durations. The parameters used in the trials and the corresponding final concentration are reported in the table 6.

Table 6: Parameters used for the GO condensation and final concentrations.

Rpm	Time, min	Wt%
2000	30	3.2
3000	30	3.6
4000	30	4.2
4000	45	4.4
4000	60	4.9

After centrifugation, effective liquid/solid phase separation was visible. This method enabled the 2.5x increase in the starting concentration, going from the initial 2% to 4.9% for 1h of centrifugation at 4000 rpm.

3.2 Bipolar membranes for DSWE

In this section, the results of the measurements and of the analysis for the direct seawater electrolysis are presented. Firstly, the morphological and chemical analyses of the nickel substrates coated with the electrocatalyst for the HER are discussed. Finally, the results of electrochemical measurements for all the different configurations of materials are reported.

3.2.1 DSWE system characterizations

Morphological characterizations

Ultraturrax-assisted coating method

A Scanning Electron Microscopy (SEM) analysis was conducted on the sintered *Ni*-felt that was coated with *NiFeCo* nanopowder using the Ultraturrax-assisted coating method. From the SEM images in figure 25, it is evident that the nanopowder coating was unevenly distributed across the surface of the *Ni*-felt, indicating a lack of homogeneity in the coating process. This result suggests that the coating solution itself may not have been uniformly dispersed.

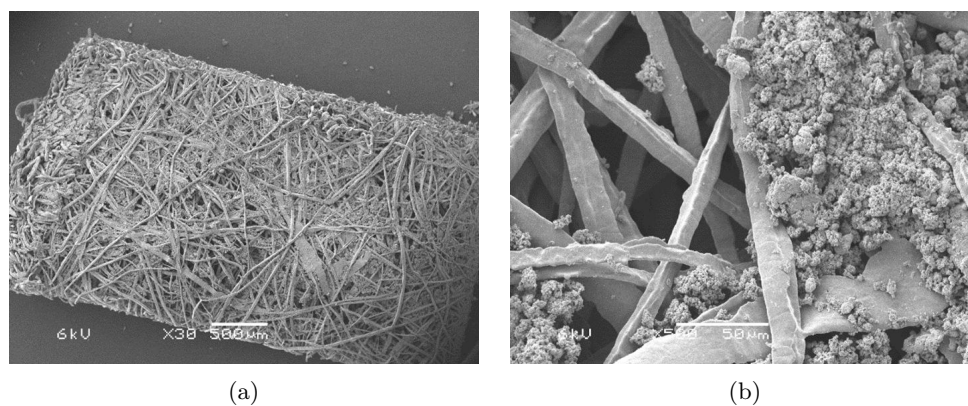


Figure 25: SEM images of the sintered nickel felt coated with a dispersion of $NiFeCo$ with Nafion, 2-propanol and SDS using the Ultraturrax-assisted coating method.

Visual observation of the dispersion used for the coating, when left undisturbed, showed a tendency for the $NiFeCo$ nanoparticles to precipitate and settle at the bottom of the container, as shown in figure 26. To mitigate this effect, we attempted to introduce the Ni -felt substrate into the solution while it was being mixed. However, this approach also did not guarantee a fully homogeneous coating, as the solution's composition could still vary during the mixing and coating process. This led to the conclusion that the $NiFeCo$ nanoparticles were not well dispersed.



Figure 26: Dispersion of $NiFeCo$ with Nafion, 2-propanol and SDS used for the Ultraturrax-assisted coating method. The nanoparticles tended to precipitate at the bottom of the container.

Furthermore, examination of the cross-sectional SEM images (figure 27) revealed that the coating did not penetrate through the Ni -felt layer. This absence of penetration could significantly hinder the catalytic performance of the $NiFeCo$ material, as a more uniform and penetrating coating would enhance its catalytic activity by increasing the accessible electrochemically active surface area.

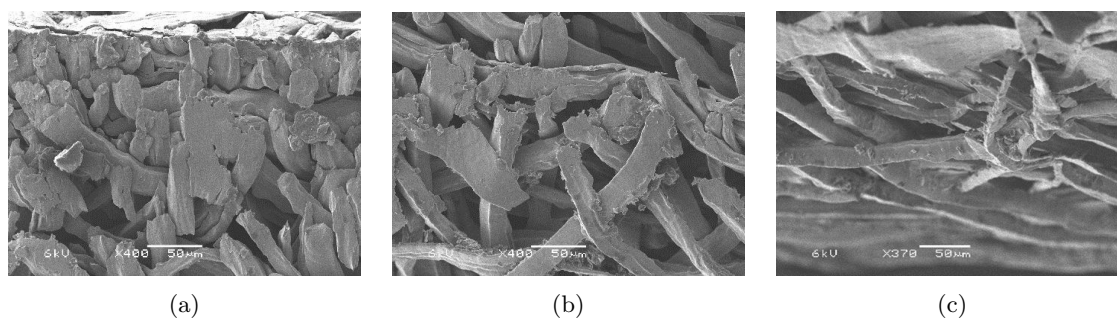


Figure 27: Cross sections SEM images of the sintered *Ni*-felt coated with the *NiFeCo* dispersion using the Ultraturrax-assisted coating method. Images show (a) the top, (b) central, and (c) bottom regions of the coated material.

Vacuum-assisted filtration coating

The vacuum-assisted filtration coating technique was used to deposit the catalyst onto the *Ni*-felt substrate. The outcome of this process is shown in figure 28a, with the corresponding SEM image provided in figure 28b. From these results, it is evident that the catalyst layer did not adhere well to the *Ni*-felt surface, as the catalyst nanoparticles easily detached. Although the particles were able to pass through the felt layer, their attachment to the substrate was insufficient. This indicates that the dispersion needs the addition of a better binding agent to improve adhesion and ensure that the catalyst remains fixed to the substrate. Furthermore, additional stirring of the catalyst dispersion did not mitigate this poor adhesion issue, suggesting that mechanical agitation alone is not sufficient to enhance coating stability. Moreover, due to the limited size of the Buchner funnel, it is not possible to coat large substrates.

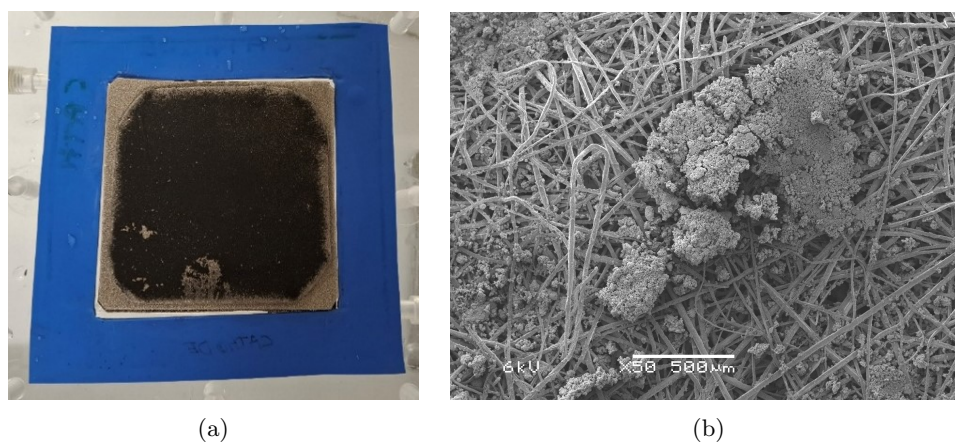


Figure 28: (a) Photo and (b) SEM image of *Ni*-felt coated with *NiFeCo* using vacuum-assisted filtration method.

Dip-coating

The dip-coating method was used to apply a catalyst layer to the *Ni*-felt, as illustrated in figure 30. This process resulted in a thin, homogeneous, red catalyst layer adhering to one side of the *Ni*-felt, as shown in figure 29a. The side facing the bottom of the glass container during the dip-coating process remained uncoated, also visible in figure 29b. The uneven coating distribution is attributed to the low-porosity of the *Ni*-felt, which prevented the catalyst solution from penetrating through the material, allowing the catalyst to adhere only to the exposed outer surface. Despite the single-sided coating, the catalyst demonstrated excellent adhesion to the *Ni*-felt. When submerged in water,

the coating remained well attached to the surface, showing no signs of detachment, as observed in figure 29c, where the water remained completely uncontaminated. This confirms the stability of the electrochemical catalyst layer produced by the dip-coating method.

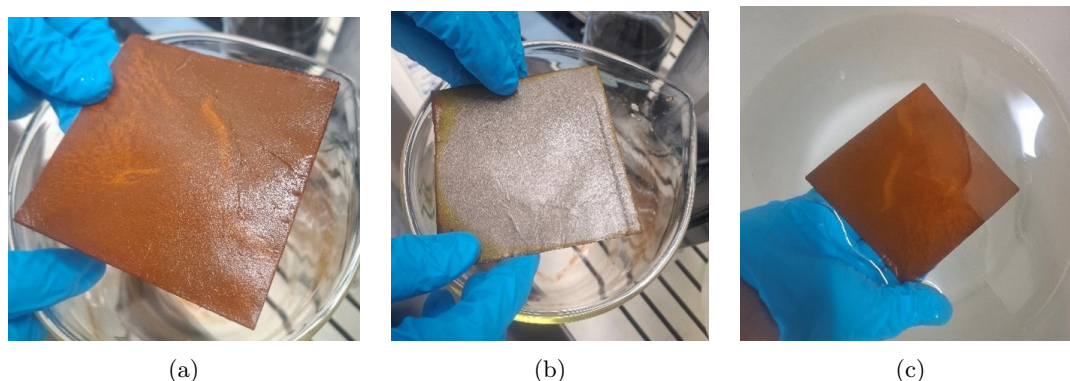


Figure 29: (a,b) Sintered *Ni*-felt coated with *NiFeCo* using dip-coating, (c) Sintered *Ni*-felt coated with *NiFeCo* using dip-coating submerged in water. No detachment is visible.

The SEM images provided valuable insights into the characteristics of the catalyst layer formed through the dip-coating technique. Figure 30a reveals that this method resulted in a much more homogeneous catalyst layer on the substrate surface. This uniform distribution of the catalyst is a significant advantage of the dip-coating process, as it ensures consistent catalytic electrochemical activity across the coated area. However, the limitations of this technique become apparent when examining the cross-section view in figure 30b. The low porosity of the *Ni*-felt substrate acts as a barrier, preventing the catalyst solution from penetrating into the inner part of the sintered *Ni*-felt material. As a result, the catalytic coating remained confined to the surface of the felt, forming a thin layer without significant internal distribution to the inner part of the sintered nickel felt. This observation aligns with the previous findings regarding the single-sided coating and explains why the catalyst is not present on the side of the felt that was in contact with the bottom of the glass container during the dip-coating process. The inability of the catalyst to penetrate the dense sintered nickel felt structure highlights a potential limitation of this coating method for applications requiring catalyst distribution throughout the inner part of the sintered nickel felt substrate.

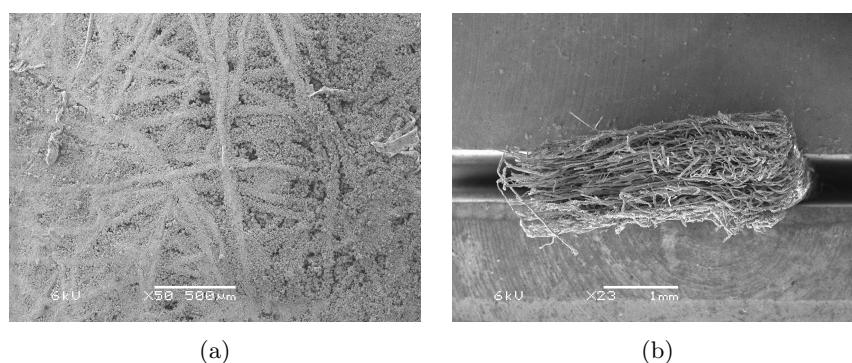


Figure 30: SEM images of the *Ni*-felt coated with *NiFeCo* using dip-coating method: (a) top view and (b) cross section.

Because of the high density and low porosity of the sintered nickel felt, the penetration of the catalyst inside the substrate was limited, regardless of the coating method employed. To ensure complete catalyst coverage throughout the Porous Transport Layer (PTL), including both external

surfaces and the internal structure, nickel foam was therefore chosen as a replacement for the sintered nickel felt substrate.

The decision to use nickel foam as a substrate for the electrocatalyst is based on the many advantages reported in literature, such as a three-dimensional structure, large specific contact area and good stability [30]. Initially, the nickel foam was horizontally placed in a small Parafilm sealed container containing the coating solution. However, in this case, the sample had almost no coating afterwards. As illustrated in Figure 31, a color change was observed on only one side of the felt, indicating that the coating process occurred exclusively on this surface. This outcome can be attributed to the small size of the container used, as well as the use of the Parafilm tape, which led to the absence of oxygen inside the container. This indicated that oxygen is necessary for the coating process. Thus, the container should not be taped with Parafilm, as otherwise no oxygen will be present, and the reactions will not occur.

The nickel foam was therefore placed in a 5L beaker glass containing the coating solution and no Parafilm tape was used. This modification allowed for a more compact coverage of the catalyst throughout the porous transport layer, including both sides and the interior.



Figure 31: *Ni*-foam (10cm x 10cm) partially coated with *NiFeCo* (right side) using dip-coating. The partial coating, highlighted by the color change, that occurred was due the absence of oxygen due to sealing flat PP container with Parafilm tape. However, the presence of oxygen gas appeared essential for the electrochemical reactions to occur.

A possible reaction mechanism of the process for the formation of the *NiFeCo* triple layered hydroxide, based on the obtained results, is presented here. It is based on the reduction of the three ions initially present in the solution, specifically Ni^{2+} , Co^{2+} , and Fe^{2+} . The ferro ions Fe^{2+} are very sensitive to oxygen gas and are oxidized to ferri ions Fe^{3+} :



The metal ions Ni^{2+} , Co^{2+} , and Fe^{2+} are reduced to the metals according to the following reactions:



Due to the presence of oxygen the non-noble metals *Ni*, *Co* and *Fe* are oxidized to their oxides:





Finally, the metal oxides react with water to yield the Triple Layered Hydroxides TLH:



According to the proposed mechanism, the final formula of the TLH as a doped compound is:



Figure 32 shows the SEM images of the TLH catalyst-coated nickel foam. A closer examination in Figure 32c reveals that the *Ni*-foam substrate is uniformly covered with "nanoflower" clusters. This microstructure closely resembles that of *NiFe* Layered Double Hydroxides (LDHs) reported in previous studies [31].

The nanoflower structure offers several advantages: it increases the available surface for catalytic reactions, providing many locations for chemical reactions to occur. These effects lead to enhanced catalytic performance. The uniform distribution of these nanoclusters on the *Ni*-foam substrate suggests a successful coating process, taking advantage of the porous nature of the foam substrate. This structure allows for better penetration and adhesion of the catalyst compared to the previously used sintered *Ni*-felt with a poor porosity. The crystalline nature of these nanoclusters is anticipated, which could further contribute to their catalytic efficiency.

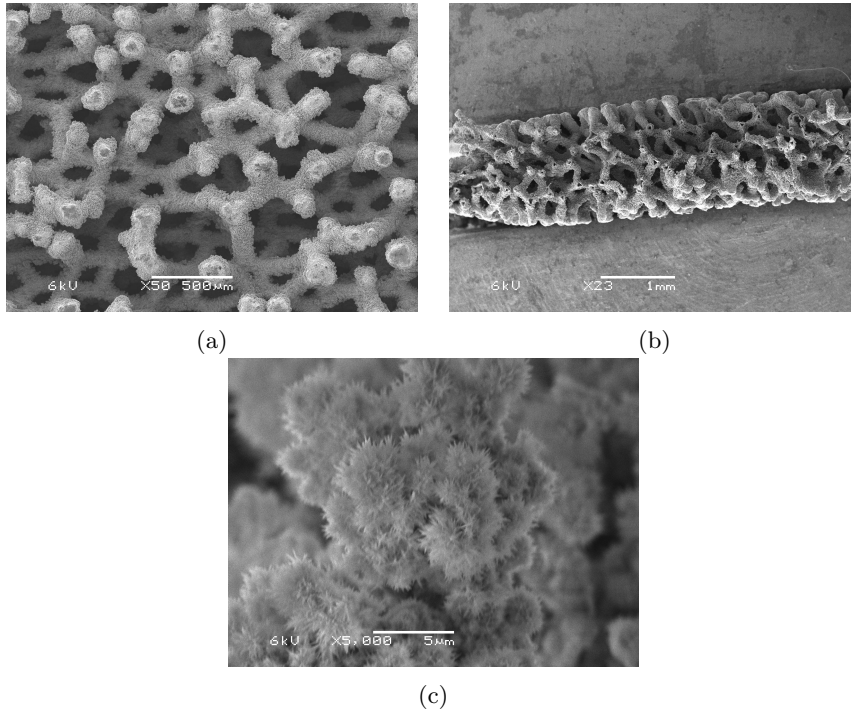


Figure 32: SEM images of the *Ni*-foam coated with *NiFeCo* TLH catalyst using dip-coating method: (a) top view and (b,c) cross section. The dip coating process lasted at least one week.

Chemical characterizations

The general composition of the catalyst deposited on the nickel substrate can be expressed as:



where x and y represent the molar fractions of Cobalt and Iron, respectively, while the remaining Nickel fraction is determined as $1 - x - y$. The presence of water is because the samples were not dried in a vacuum environment after the dip-coating process.

From the Energy Dispersive X-ray (EDX) analysis, we can infer that the synthesized Triple-layered Hydroxide (TLH) is not composed of pure individual phases but rather forms a doped structure where Fe , Co , and Ni are mixed.

The molar fractions of Fe , Co , and Ni were determined based on the elemental composition obtained from EDX, reported in table 7.

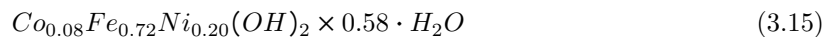
Table 7: EDX spectrum of (a) nickel felt and (b) nickel foam coated with $NiFeCo$ using the dip-coating method.

Element	<i>Ni-felt</i>	<i>Ni-foam</i>
<i>O</i> , wt%	41.3 ± 0.3	39.6 ± 0.4
<i>Fe</i> , wt%	40.1 ± 0.4	40.8 ± 0.4
<i>Ni</i> , wt%	11.6 ± 0.3	14.6 ± 0.4
<i>Co</i> , wt%	4.8 ± 0.3	3.6 ± 0.3
<i>Cl</i> , wt%	1.4 ± 0.1	1.1 ± 0.1
<i>S</i> , wt%	0.7 ± 0.1	0.3 ± 0.1
<i>Si</i> , wt%	0.2 ± 0.0	-

Since EDX provides weight percentages of each element, we assume a total sample mass of 100g. This allows us to directly interpret the reported weight percentages as grams of each component. Using the molar mass of each element (Co : 58.93g/mol, Fe : 55.85g/mol, Ni : 58.69g/mol, O : 16.00g/mol), the number of moles n_i for each element was determined as:

$$n_i = \frac{m_i}{M_i} \quad (3.14)$$

where m_i is the mass of the element obtained from EDX (in grams), and M_i is its molar mass. The remaining fraction of oxygen was attributed to the remaining hydrated water content in the sample. This molar fraction for water was defined as w , representing the number of moles of H_2O associated with the compound. The calculated molar fractions for the *Ni-felt* and *Ni-foam* substrates are used to determine the final chemical composition of the coated compound, described by the following formulas, respectively:



As expected, the molar fraction of nickel was found to be represented by $1 - x - y$, validating our assumptions. The presence of water confirms that the samples retained still some moisture due to the absence of vacuum drying after dip-coating. The hydrogen is not present in the EDX tables because its weight is too low to be detected. The table 8 summarizes the calculations explained.

Comparing the results for *Ni-felt* and *Ni-foam*, we observe nearly identical compositions, except for the Co content, which is slightly higher for the sintered *Ni-felt*. This suggests that sintered *Ni-felt* may exhibit enhanced catalytic activity, potentially making it a more effective substrate for hydrogen evolution reactions as cobalt has higher catalytic activity for HER.

Table 8: Summary of the elemental composition obtained from the EDX analysis for *Ni*-felt and *Ni*-foam substrates. The reported mass values were used to calculate the molar fractions of *Co*, *Fe* and *Ni* in the TLH catalyst deposited on each substrate. The calculated molarity of each element is also included.

	<i>Ni</i> -felt	<i>Ni</i> -foam	molar mass	molarity for <i>Ni</i> -felt	molarity for <i>Ni</i> -foam
O	41.3 g	39.6 g	15.9994 g/mol	2.58 mol	2.48 mol
Ni	11.6 g	14.6 g	58.6934 g/mol	0.20 mol	0.25 mol
Fe	40.1 g	40.8 g	55.8450 g/mol	0.72 mol	0.73 mol
Co	4.8 g	3.6 g	58.9332 g/mol	0.08 mol	0.06 mol

Electrochemical characterizations

The bipolar membrane electrolysis runs for the tests were performed at $1000A/m^2$ four times, each lasting four hours, with a sampling time of one second.

First test

In the first test no electrocatalyst was applied on the *Ni*-foam at the anode side and at the cathode side. At $1000A/m^2$ and $30.0\text{ }^\circ\text{C}$, the bipolar membrane electrolysis cell had a cell voltage of 3.6V.

The measured values of the BPM voltage must be corrected in case two different reference electrodes are used. The reference electrodes used in the first test were *Ag/AgCl* (3M *KCl*) on the cathode side and *Hg/HgO* (1M *KOH*) on the anode side. Therefore:

$$E_{BPM} = E_{measured} - b.E \quad (3.17)$$

Where $E_{measured}$ is the potential measured across both reference electrodes and $b.E$ is the correction factor. To calculate the correction factor, we consider that the bipolar membrane voltages E_{BPM} measured for the different tests should be the same since the BPM used is the same in all the tests. From the difference of the bipolar membrane voltage of the first test, measured using *Ag/AgCl* (3M *KCl*) and *Hg/HgO* (1M *KOH*) as reference electrode, and the arithmetic mean of the bipolar membrane voltage of the other tests, measured using two identical *Hg/HgO* (1M *KOH*) reference electrodes, we can calculate the correction factor $b.E$:

$$b.E = E_{BPM,Hg/HgO} - E_{BPM,Ag/AgCl} \quad (3.18)$$

The bipolar membrane voltage (figure 33) remained stable throughout the measuring time. The corrected measured voltage across the bipolar membrane increased slowly from 1.06V to 1.17V. This gradual increase may be attributed to a rise in the anolyte and catholyte concentrations during the tests due to the consumption of water during electrolysis, as the feed of pure water through the osmose cell may still not be activated due to too low difference in water vapor pressure between the 0.5M *NaCl* solution and the *Na₂SO₄* catholyte. This increase of cell voltage is a repeated result during all the measurements. The final averaged potential drop across the BPM was 1.12V, which aligns with the specifications provided in the Fumatech datasheet for the BPM used.

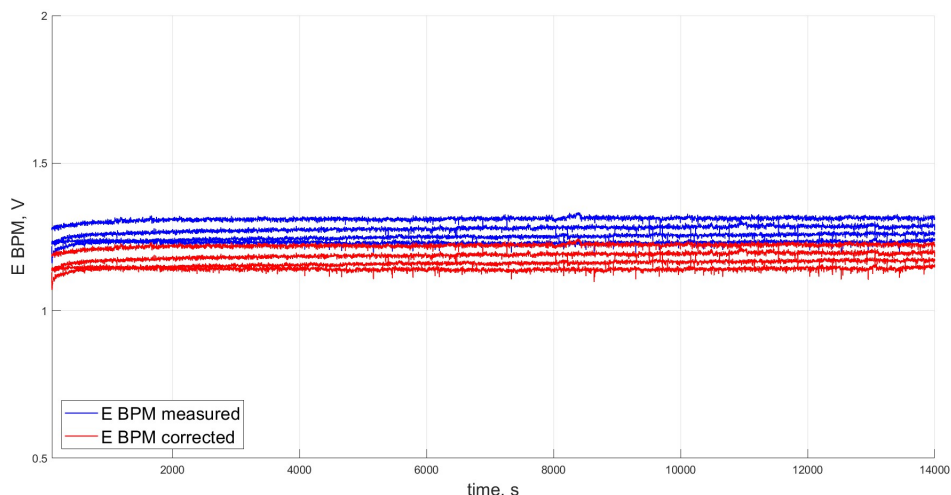


Figure 33: Voltage drop across the Fumatech BPM at $1000A/m^2$. The blue lines are the measured potential difference across the bipolar membrane at $1000A/m^2$ using two different reference electrodes ($Ag/AgCl$ (3M KCl) and Hg/HgO (1M KOH)). In contrast, the red lines show the corrected potential difference across the Fumatech BPM at $1000A/m^2$. The anolyte was 1M $NaOH$ solution at the start, while the catholyte was 1M Na_2SO_4 solution at the start. During electrolysis, the concentration of the anolyte and catholyte increased due to the consumption of water during electrolysis.

The introduction of an active electrocatalyst layers for the anode and the cathode should reduce E_{cell} to reach the target of the European Union of 2.0V at $5000A/m^2$.

Second test

Runs at $1000A/m^2$ for the second test revealed however unexpected behavior: the cathode potential was more negative than for pure Ni -foam while the bipolar membrane voltage was too low, namely 0.6V. Therefore, the cell was directly disassembled. It was found that the compression at the cathode side was too high. The five platinum coated Ti -mesh layers of $150\mu m$ each were therefore removed. However, after an initial electrolysis run, we observed that an anode potential that was stable and remained at 1.0V vs Hg/HgO (1M KOH), while the cathode potential exceeded $-2V$ vs the reference electrode $Ag/AgCl$ (1M KCl) (figure 34a). Recording of the cathode potential was not therefore feasible as the measurable range of the IVIUM Peripheral Differential Amplifier was $-2V$. Furthermore, the voltage across the bipolar membrane was too low (around 0.6V at $1000A/m^2$) and floating. This bipolar membrane voltage instability may have resulted from the fact that the bipolar membrane was not flat but wrinkled, which created varying distances between the anode and cathode layers (figure 34b).

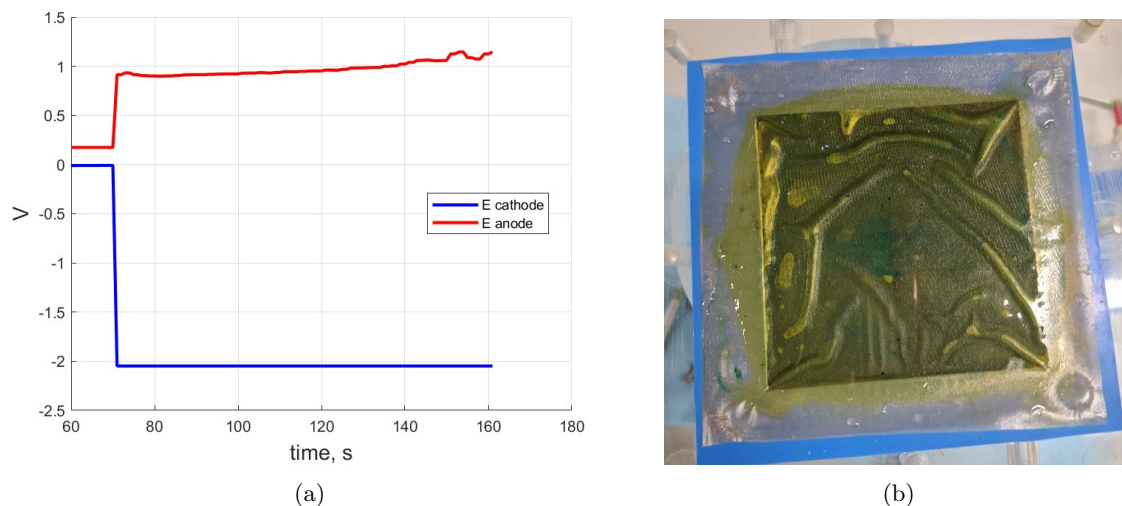


Figure 34: (a) Anode and cathode potentials after the run at $1000\text{A}/\text{m}^2$ of the electrolyser cell with five layers of titanium fiber felt ($175\mu\text{m}$) coated with $10\text{g}/\text{m}^2$ *Ir*-MMO at the anode and five layers of titanium mesh ($150\mu\text{m}$) coated with $60\text{g}/\text{m}^2$ of platinum at the cathode (second test). Anode potential was stable around 1.0V , while the cathode potential exceeded the recording limit of IVIUM software of -2V ; (b) autopsy of the instable bipolar membrane electrolysis cell of the second test. BPM showed wrinkling after the run.

Third test

Using a sintered titanium felt coated with *Ir*-MMO both at the anode and cathode side also resulted in an out-of-range cathode potential. However, the anode potential was stable, hence, from this moment on, we focus only the optimization of the cathode side.

Fourth test

Autopsy of the electrolysis cell after the electrochemical characterization of the fourth test revealed that not all five layers of $150\mu\text{m}$ platinized *Ti*-mesh current collector still had the gray color of platinum anymore (figure 35). This points towards a high pH that was present on the black-colored platinized $150\mu\text{m}$ *Ti*-mesh. Another issue was the high mechanical pressure at the cathode side. This was caused by too high compression of the *Ni*-foam added to make electrical contact. It is important to note that, during the experiment, the cathode potential was observed to be excessively negative, indicating a potential issue that may need further investigation.

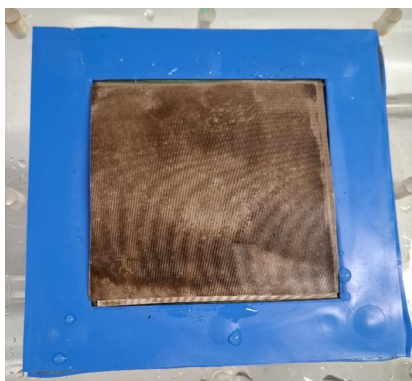


Figure 35: Black-colored platinized $150\mu\text{m}$ *Ti*-mesh due to a high pH at the cathode side.

Fifth test

The thin platinized *Ti*-mesh electrodes of $150\mu\text{m}$ were not introduced again as the hydrodynamic resistance of these thin electrodes in the longitudinal direction (not perpendicular flow) is likely too high. It was found experimentally that highly porous *Ni*-foam at the cathode gave much better performance as a cathode. The recorded cell voltage was 3.3V at $1000\text{A}/\text{m}^2$ at $30.0\text{ }^\circ\text{C}$.

The configuration of the fifth test was chosen as starting point to analyze three methods for the coating of the catalyst on the nickel substrate: Ultraturrax-assisted coating, vacuum-assisted filtration coating and dip-coating.

The cell voltage and the BPM voltage for the four-hour runs carried out at $1000\text{A}/\text{m}^2$ for bipolar membrane electrolysis controlled at $30.0\text{ }^\circ\text{C}$ are reported in the table 9. The anolyte at start was 1.0M NaOH and $1.0\text{ M Na}_2\text{SO}_4$ was used as catholyte. As the anode, five $175\mu\text{m}$ layers of $10\text{g}/\text{m}^2$ platinum-iridium MMO coated titanium foam were used (total thickness of five layers was 0.89mm). The electrode dimensions were $10\text{cm} \times 10\text{cm}$ for the anode and the cathode. The pump speed of the anolyte and catholyte was $600\text{mL}/\text{min}$. At the start, the osmose cell was supplied with 0.5M NaCl solution pumped at $600\text{mL}/\text{min}$. The bipolar membrane was standard FBM (Fumatech, Germany). The osmose cell used a porous PTFE layer (POREX, PGM 25).

Using the **ultraturrax-assisted coating**, the cell potential was reduced to 3.32V .

In the case of the **vacuum-assisted filtration coating** method, the four-hour run was performed only once since the cell potential was increasing with respect to the previous case. This can be explained by the complete detaching of the nanoparticle of the catalyst from the surface of the sintered nickel felt substrate.

The results obtained using the **dip-coating** method are the same regardless of whether a *Ni*-foam or sintered *Ni*-felt substrate is used, contrary to our expectations. Moreover, the results remain stable over the four measurements, with lower standard deviations compared to previous experiments.

In this table, each row corresponds to a different electrolyser cell, identified based on the characteristics of the electrocatalyst at the cathode. The table reports the standard deviations for each result, except for those corresponding to the vacuum-assisted filtration coating. This is because the results obtained with this method were already worse than the previous ones from the first test, leading to the decision not to perform additional measurements.

Table 9: Summary of four-hour test results for the six electrolyser cell configurations carried out at $1000\text{A}/\text{m}^2$ for bipolar membrane electrolysis controlled at $30.0\text{ }^\circ\text{C}$ for different methods for coating the catalyst for the HER at the cathode. Each row represents the average value of four runs for an electrolyser cell configuration characterized by the electrocatalyst applied at the cathode. The table reports the measured cell potentials and BPM potentials.

Cathode electrocatalyst	$E_{\text{cell}}, \text{V}$	E_{BPM}, V
Pure <i>Ni</i> -foam without electrocatalyst	3.66 ± 0.06	1.27 ± 0.05
Thin platinized <i>Ti</i> -mesh	3.42 ± 0.05	1.20 ± 0.01
Ultraturrax <i>NiFeCo</i> nanoparticle dip	3.32 ± 0.05	1.14 ± 0.02
<i>NiFeCo</i> coating in Buchner funnel	3.43	1.18
Dip coating <i>Ni</i> -felt (<i>Ni,Fe,Co</i>) Cl_2	3.41 ± 0.02	1.18 ± 0.01
Dip coating <i>Ni</i> -foam (<i>Ni,Fe,Co</i>) Cl_2	3.40 ± 0.05	1.19 ± 0.02

From these bipolar membrane voltages and from equation (3.18), we can calculate the correction term $b.E$:

$$b.E = 1.27\text{V} - 1.18\text{V} = 0.09\text{V} \quad (3.19)$$

Hence, the voltage drop across the bipolar membrane vs Hg/HgO (1M KOH) reference electrode for the pure Ni -foam without electrocatalyst can be corrected as:

$$E_{BPM} = 1.27V - 0.09V = 1.18V \quad (3.20)$$

Similarly, the cathode potential of the electrolyser cell with pure nickel foam without electrocatalyst as cathode is calculated as:

$$E_{cathode} = E_{measured} + 0.09V = -1.42V + 0.09V \quad (3.21)$$

where $E_{cathode}$ is the cathode potential vs Hg/HgO (1M KOH) reference electrode and $E_{measured}$ is the cathode potential measured vs $Ag/AgCl$ (3M KCl). The anode and cathode potentials vs Hg/HgO (1M KOH) for each electrolyser cell configuration are reported in the table 10.

Table 10: Summary of four-hour test results for the six electrolyser cell configurations carried out at $1000A/m^2$ for bipolar membrane electrolysis controlled at $30.0\text{ }^\circ\text{C}$ for different methods for coating the catalyst for the HER at the cathode. Each row represents the average value of four runs for an electrolyser cell configuration characterized by the electrocatalyst applied at the cathode. The table reports the anode and cathode potential vs Hg/HgO (1M KOH) reference electrode.

Cathode electrocatalyst	$E_{cathode}, \text{ V}$	$E_{anode}, \text{ V}$
Pure Ni -foam without electrocatalyst	-1.33 ± 0.02	0.99 ± 0.02
Thin platinized Ti -mesh	-1.37 ± 0.04	0.85 ± 0.02
Ultraturrax $NiFeCo$ nanoparticle dip	-1.33 ± 0.02	0.85 ± 0.01
$NiFeCo$ coating in Buchner funnel	-1.37	0.89
Dip coating Ni -felt (Ni, Fe, Co) Cl_2	-1.33 ± 0.01	0.90 ± 0.01
Dip coating Ni -foam (Ni, Fe, Co) Cl_2	-1.32 ± 0.01	0.89 ± 0.02

The plots reported in figure 36 present the test results of the four hour runs for each electrolyser cell configuration. These plots specifically display the cell voltage, as the focus of this study is the cell voltage reduction through the introduction of the electrocatalyst for HER at the cathode.

Each plot contains four curves representing the evolution of the cell potential over four hours for each of the four tests. However, as observed in the plots, some data points are missing due to issues with the IVIUM software, which failed to record data for the entire duration of the tests in certain cases. For the vacuum-assisted coating, only one curve is shown because, as previously mentioned, the initial test results were already worse than those of other methods, leading to the decision not to conduct additional measurements.

Moreover, the plots clearly show that the cell voltage in the last run is consistently higher than in previous tests. This trend is observed across all experiments and can be attributed to the a rise in the anolyte and catholyte concentrations during the tests due to the consumption of water during electrolysis over successive runs.

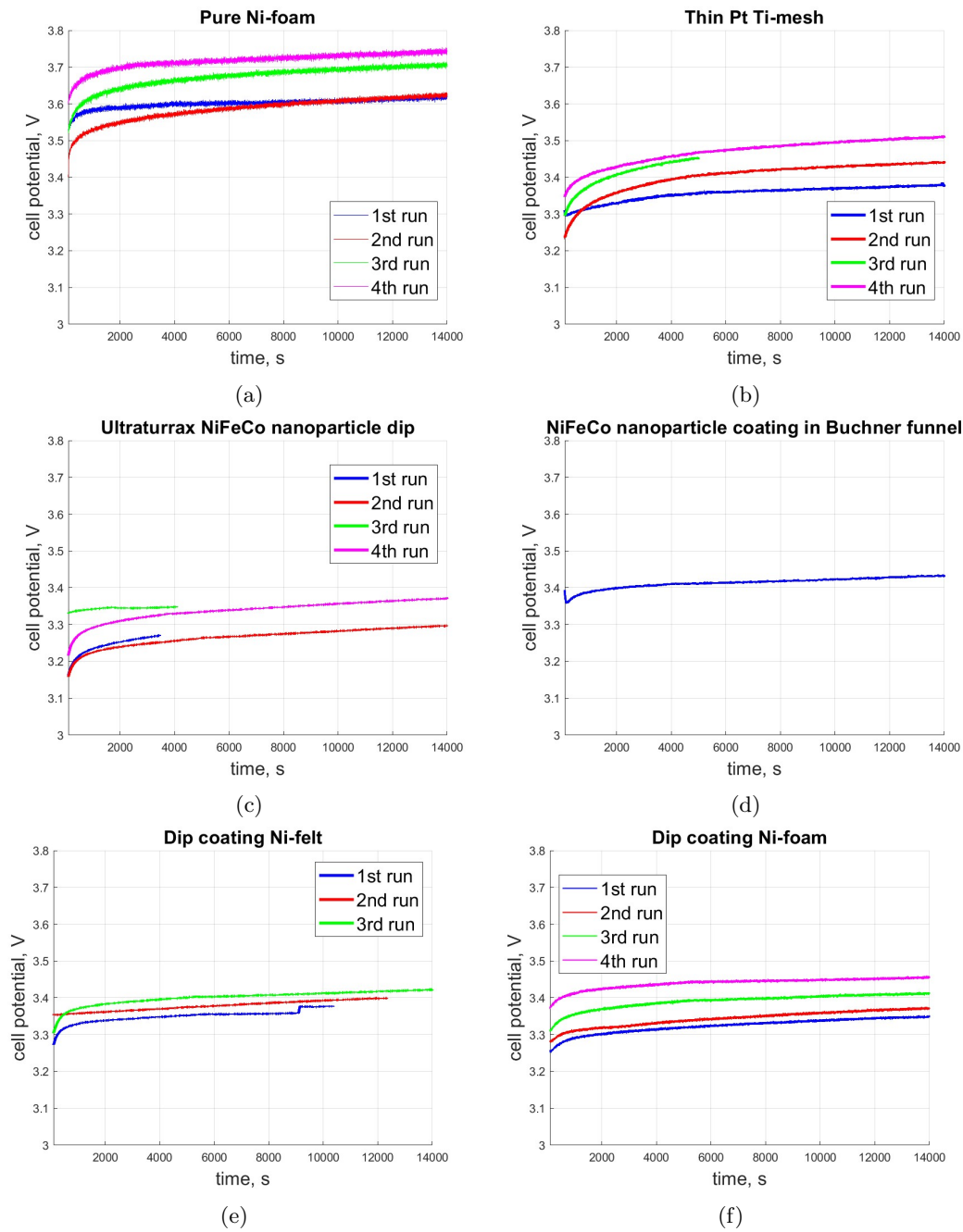


Figure 36: Evolution of cell voltage over time for different cathode compositions of the electrolyzer cell. (a) Pure nickel foam without electrocatalyst; (b) Thin platinumized titanium mesh; (c) Ultraturrax $NiFeCo$ nanoparticle dip; (d) $NiFeCo$ coating in Buchner funnel; (e) Dip coating Ni -felt (Ni,Fe,Co) Cl_2 ; (f) Dip coating Ni -foam (Ni,Fe,Co) Cl_2 .

For a better comparison, figure 37 presents a comparative analysis of cell voltage across different experimental setups, with each data point representing the mean cell voltage and its corresponding standard deviation. The x-axis labels indicate the different experimental conditions tested. As expected, the addition of HER catalyst for the cathode and OER catalyst for the anode generally results in a reduction of cell voltage compared to the *pure Ni-foam* baseline. The errors bars are comparable in the tests, except for the sintered Ni -felt coated with the dip-coating method, indicating that

the reason behind the increase of the cell voltage is the same, namely the increase of the anolyte and catholyte concentration due to water depletion. The *Buchner funnel* condition lacks error bars, since only a single experimental run was conducted for this setup. Future studies should focus on longer-term stability tests under controlled water supply to determine the true performance limitations of each condition and to provide more robust error bars. Notably, the Ultraturrax-assisted coating method of *NiFeCo* nanoparticles with Nafion binder achieved the lowest cell voltage. This result contrasts with our initial expectation that the *Ni*-foam substrate would yield the best performance based on SEM analysis. This may be due to the porous structure of the *Ni*-foam, which generally is advantageous. However, in this case, the sintered nickel felt showed higher catalytic activity due to the coated commercial *NiFeCo* nanoparticle sized electrocatalyst, despite the fact that only the outer surface area was coated.

The figure also reports the Voltage Efficiency (VE) for each experiment, calculated according to the equation (2.5).

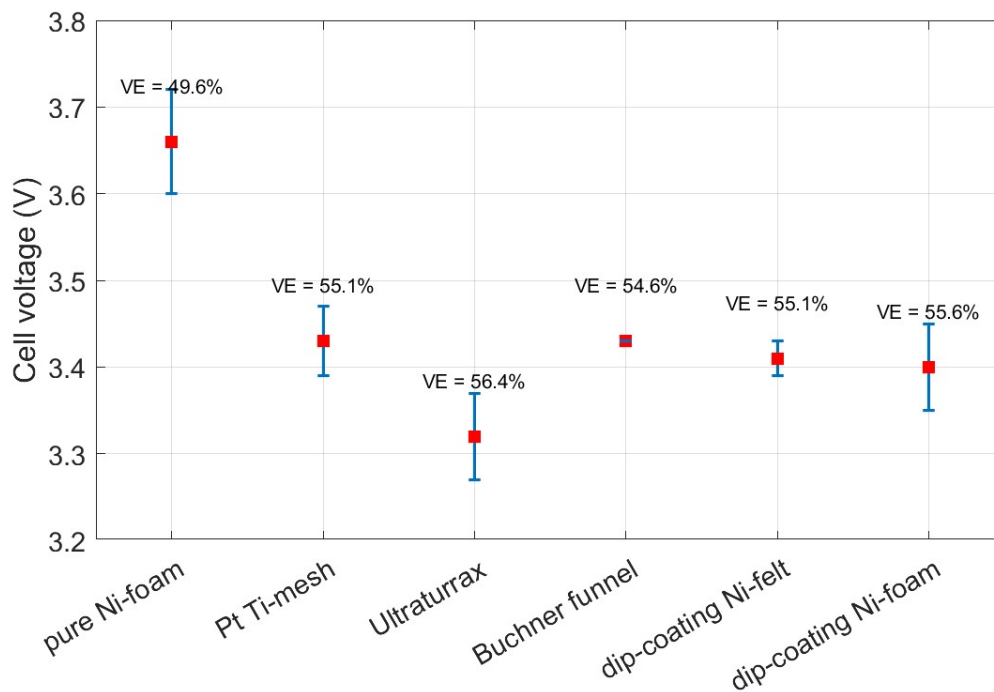


Figure 37: Comparison of cell voltage and voltage efficiency for different cathode side configuration. Error bars represent standard deviation across multiple experimental runs, except for the *Buchner funnel* method, which was conducted only once.

Figure 38 presents the anode and cathode potential evolution over time for the fourth run of the analyzed electrolyser cells, illustrating the influence of various electrocatalyst modifications on electrode potentials. The data indicates that electrocatalyst modifications had the most significant impact on the anode potential, resulting in a substantial reduction in anode potential. Specifically, the electrolyser cell configuration utilizing five layers of *Ti*-felt coated with *Pt-Ir* MMO as the anode and a cathode PTL composed of a stack of *Ni*-foam with a total thickness of 1.7mm and a 1.4mm *Ni*-felt coated with *NiFeCo* via the Ultraturrax-assisted method exhibited the lowest cathode overpotential. Similar cathode potentials were achieved using the dip-coating method, regardless of the substrate material employed. Substitution of the *Ni*-felt with *Ni*-foam as the substrate for dip-coating did not provide a lower cathode overpotential. However, the dip-coating of *Ni*-foam resulted in more stable

cathode potentials with reduced fluctuations.

Based on the data, the inclusion of a catalyst did not substantially lower the cathode overpotential. The largest reduction in cathode overpotential was 0.1V, while a reduction of 0.14V was observed for the anode overpotential.

In particular, the electrolyser cell employing five layers of *Ti*-felt coated with *Pt – Ir* MMO as the anode and a stack of *Ni*-foam layers with a total thickness of 3.1mm (*Pt Ti-mesh*) exhibited unstable cathode potential behavior, becoming increasingly negative over time. During the final hour of operation, the fifth configuration cathode potential coincided with the performance observed without catalyst, indicating instability and the need for further optimization of this cathode configuration. Consequently, this cathode configuration was modified by substituting one of the *Ni*-foam layers with a *Ni* substrate coated with *NiFeCo*-based catalyst using alternative coating methods. On the cathode side, the most stable potentials were observed with the dip-coating of *Ni*-foam. However, the lowest cathode potential was obtained with the dip-coating of the sintered nickel felt.

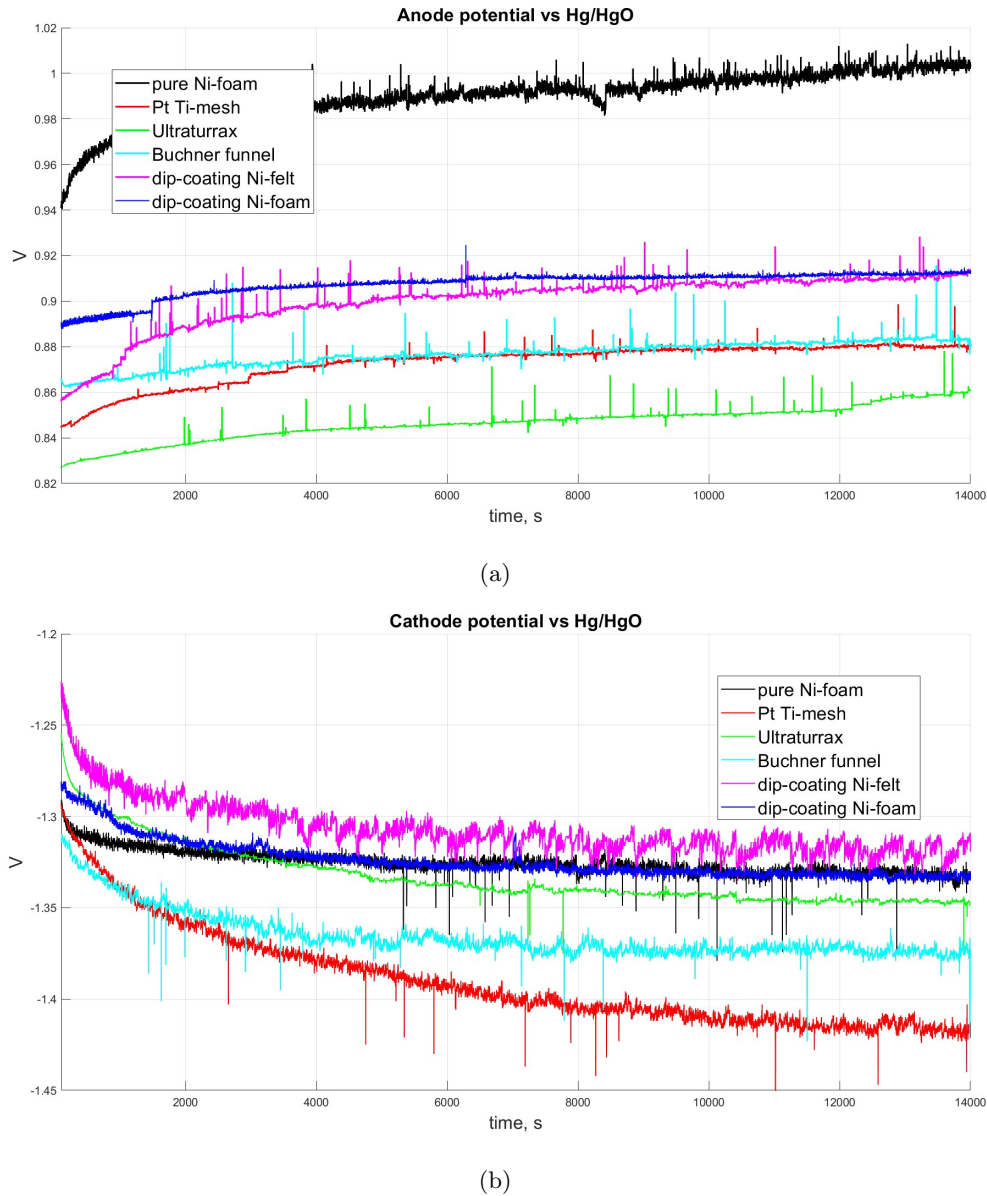


Figure 38: Evolution of the (a) anode potential and (b) cathode potential vs Hg/HgO (1M KOH) over time for the different electrolyser cell configuration. The data reported correspond to the fourth run for each experiment.

The electrochemical measurements, reported in figure 38, reveal that the cathode potentials obtained via chronopotentiometry were significantly lower than $-1.0V$. If hydrogen evolution was proceeding via a proton reduction mechanism (equation (2.9)), as we assumed, we would expect much less negative cathode potentials. Since the observed cathode potentials were much more negative than the thermodynamic requirements for proton reduction, the water reduction is regarded as the most dominant cathodic reaction.

The water reduction is given by:



Considering the Nernst equation applied to the water reduction reaction:

$$E_{cathode} = E_{(H_2O, H_2)}^0 + \frac{RT}{4F} \cdot \ln \left(\frac{a_{H_2O}}{p_{H_2}^2 \cdot a_{OH^-}^4} \right) \quad (3.23)$$

where $E_{(H_2O, H_2)}^0 = -0.828V$ vs NHE, the gas constant $R = 8.331J/(mol \cdot K)$ and the Faraday constant $F = 96486C \cdot mol^{-1}$, with $T = 303K$, and assuming the water activity $a_{H_2O} = 1$ and the hydrogen partial pressure $p_{H_2} = 1atm$. Given that the measured pH of the catholyte at the end of the tests was 13.4, we can calculate the OH^- activity as following:

$$a_{OH^-} = (f_{OH^-} \cdot c_{OH^-}) \quad (3.24)$$

where the molar activity coefficient $f_{OH^-} = 0.75$ [32] and $c_{OH^-} = \frac{10^{-6}mol}{L} = 0.251 \frac{mol}{L}$, leading to $a_{OH^-} = 0.1884$. Finally, substituting these results in equation (3.23):

$$E_{cathode} = -0.828 + \frac{8.331 \cdot 303}{4 \cdot 96486} \cdot \ln \left(\frac{1^4}{1^4 \cdot 0.1884^4} \right) = (-0.828 + 0.0437)V \quad (3.25)$$

$$E_{cathode} = -0.7843V \quad vs NHE \quad (3.26)$$

The cathode potential at zero current as calculated is $-0.8823V$ versus the reference electrode Hg/HgO (1M KOH). This is true for an absolute temperature of 303K and a pH of 13.4. In practice, the cathode potential at $1000A/m^2$ was measured vs Hg/HgO (1M KOH) reference electrode, meaning that we can calculate the cathode overpotential as the difference between the calculated cathode potential of $-0.8823V$ and the measured cathode potential vs Hg/HgO (1M KOH):

$$\eta_{cathode} = (-0.8823 - E_{CATHODEmeasured,vsHg/HgO})V \quad (3.27)$$

The anode reaction is given by:



The anode potential is given by:

$$E_{anode} = E_{(OH^-, O_2)}^0 + \frac{RT}{4F} \cdot \ln \left(\frac{p_{O_2} \cdot a_{H_2O}^2}{a_{OH^-}^4} \right) \quad (3.29)$$

where $a_{OH^-} = 0.7$ and $E_{(OH^-, O_2)}^0 = 0.404V$ vs NHE, leading to:

$$E_{anode} = 0.404V + 0.00933V = 0.4133V, \quad vs \quad NHE \quad (3.30)$$

The anode overpotential can be calculated as the difference between the measured anode potential vs Hg/HgO (1M KOH) and the calculated potential of the anode vs Hg/HgO (1M KOH) at zero current. The anode potential at zero current at the measured pH = 13.4 of the anolyte at 30.0 °C is 0.4133V vs NHE or equal to 0.3153V vs Hg/HgO (1M KOH). This is expressed in the equation:

$$\eta_{anode} = E_{measured,vsNHE} - (+0.4133V) = E_{measured,vsHg/HgO} - 0.3153V \quad (3.31)$$

The resulting cathode and anode overpotentials are summarized in the table 11. The lower anode and cathode overpotentials of the electrolyser cells which incorporate electrocatalysts means that the electrochemical reaction is occurring more efficiently. This indicate, once again, that the electrocatalyst used in this study are effective in reducing the activation energy of the HER and OER processes.

In the first test, when no electrocatalysts were added, the cathode potential was measured vs $Ag/AgCl$

(3M KCl) reference electrode. Thus, in this case, the cathode overpotential is calculated as:

$$\eta_{cathode} = E_{measured,vsNHE} - (-0.7843V) = E_{measured,vsAg/AgCl} + 0.9813V \quad (3.32)$$

Being $E_{Ag/AgCl}^0 = +0.197V$ vs NHE.

Table 11: Cathode and anode overpotential calculated according to equation (3.27) and (3.31) and assuming water reduction at the cathode. Condition: $1000A/m^2$ and operated at $30.0^\circ C$ in $1M Na_2SO_4$ at $pH = 13.4$

Cathode electrocatalyst	$\eta_{cathode}, V$	η_{anode}, V	Anode electrocatalyst
Pure <i>Ni</i> -foam without electrocatalyst	-0.44	0.68	Pure <i>Ni</i> -foam without electrocatalyst
Thin platinized titanium mesh	-0.49	0.54	5 layers <i>Pt - Ir</i> MMO on sintered <i>Ti</i> -felt
Ultraturrax <i>NiFeCo</i> nanoparticle dip	-0.45	0.54	5 layers <i>Pt - Ir</i> MMO on sintered <i>Ti</i> -felt
<i>NiFeCo</i> coating in Buchner funnel	-0.49	0.58	5 layers <i>Pt - Ir</i> MMO on sintered <i>Ti</i> -felt
Dip coating <i>Ni</i> -felt in (<i>Ni,Fe,Co</i>) Cl_2 solution	-0.45	0.59	5 layers <i>Pt - Ir</i> MMO on sintered <i>Ti</i> -felt
Dip coating <i>Ni</i> -foam in (<i>Ni,Fe,Co</i>) Cl_2 solution	-0.44	0.58	5 layers <i>Pt - Ir</i> MMO on sintered <i>Ti</i> -felt

To compare the values obtained in our study with those in the literature, it is essential to consider the setup of the Alkaline Water Electrolysis (AWE) system, which does not use a membrane. Consequently, the cell potential E_{cell} is lower because it lacks the contribution of the membrane potential E_{BPM} . In contrast, in a system with a bipolar membrane, the cell potential is determined by the sum of the anode potential, cathode potential, and membrane potential:

$$E_{cell} = (E_{anode} - E_{cathode}) + E_{BPM} \quad (3.33)$$

In the table 12, we report the anode-cathode potential difference ($E_{anode} - E_{cathode}$), comparable to the cell potential of AWE systems, the BPM potential (E_{BPM}), and the cell potential (E_{cell}). By adding the membrane potential to the anode-cathode potential difference, we obtain a value that closely approximates the cell potential. It is also important to consider that all values were measured at $30.0^\circ C$, since temperature significantly influences the cell potential. In particular, higher temperatures reduce the thermodynamic potential required for water splitting.

Table 12: Comparison of cell potentials in alkaline water electrolysis and bipolar membrane systems. The AWE cell potential is calculated as the difference between the anode and cathode potentials of the DSWE system with BPM, while the BPM cell potential includes the additional contribution of the membrane potential.

Cathode electrocatalyst	$E_{anode} - E_{cathode}, V$	E_{BPM}, V	E_{cell}, V
Pure <i>Ni</i> -foam without electrocatalyst	2.32	1.27	3.66
Thin platinized <i>Ti</i> -mesh	2.22	1.20	3.42
Ultraturrax <i>NiFeCo</i> nanoparticle dip	2.18	1.14	3.32
<i>NiFeCo</i> coating in Buchner funnel	2.26	1.18	3.43
Dip coating <i>Ni</i> -felt (<i>Ni,Fe,Co</i>) Cl_2	2.23	1.18	3.41
Dip coating <i>Ni</i> -foam (<i>Ni,Fe,Co</i>) Cl_2	2.21	1.19	3.40

The values presented in the table 12 demonstrate that the cell potentials, calculated as $E_{anode} - E_{cathode}$, obtained through the direct seawater electrolysis using bipolar membranes that is employed in this thesis, are comparable to those of a conventional Alkaline Water Electrolysis (AWE) system, which typically operates within the range of 1.84–2.25 V under standard conditions [33]. This result suggests that the BPM-based seawater electrolysis approach achieves performance comparable with AWE technologies, even when utilizing seawater as the feedstock.

Conclusions

Blue Energy, or energy harvested from salinity gradients, represents a promising renewable source with significant potential to contribute to the transition toward a sustainable energy future. Among the available technologies, Reverse Electrodialysis (RED) has proven particularly effective for harvesting this energy, thanks to its ability to convert the concentration gradient between seawater and freshwater into electrical power. The integration of advanced materials like Graphene Oxide (GO) into Ion Exchange Membranes (IEMs) has significantly enhanced the efficiency of this technology.

This study presents an investigation into Graphene Oxide (GO)-based Ion Exchange Membranes (IEMs) for Reverse Electrodialysis (RED) technology, focusing on fabrication, performance optimization, and scalability. By incorporating Aramid NanoFibers (ANF) in Meta (Nomex) configuration as reinforcement, we engineered membranes with enhanced conductivity without compromising thickness. The optimal formulation of 15mg GO with 25% ANF achieved good performance: 90.7% permselectivity and a low ionic resistance of $2.7\Omega \cdot cm^2$. The ionic resistance value is lower than those reported in similar work in GO-based membrane. However, the permselectivity achieved with these GO-based membranes are still worse than the one obtained in other similar studies.

The fixed membrane dimension of the dead-end fabrication method used in this study highlights a significant limitation of the current fabrication method, which restrict scalability but allows for a great control on the properties and morphology of the membrane. The ongoing research and development efforts are expected to overcome current limitations and enable the large-scale application of this technology, contributing to the transition towards a sustainable energy future. A promising technique for large-scale production of these membranes is Roll-to-Roll (R2R) processing, which can be highly effective if a homogeneous solution with appropriate viscosity can be achieved.

The increasing global demand for clean energy has also driven the search for sustainable fuel alternatives. Hydrogen, with its high energy density and zero-emission combustion, presents a promising energy carrier. However, the environmental footprint of hydrogen production depends on the methods employed, with conventional techniques contributing substantially to CO_2 emissions. Direct seawater electrolysis offers an interesting alternative to hydrogen production, especially in regions where seawater is abundant.

This thesis focused on direct seawater electrolysis using a Bipolar Membrane (BPM) as a separator. Compared to indirect methods involving desalination, direct seawater electrolysis does not need desalination of seawater to ultra-pure water. However, it faces challenges, including mineral scale formation and electrode corrosion. Bipolar membrane electrolysis offers a promising approach, creating localized pH conditions that create the optimal condition for the HER and OER processes.

The central objective of this work was to investigate the impact of electrocatalyst addition on the performance of a BPM-based direct seawater electrolyser. Various catalyst materials and coating

deposition methods were explored to minimize the bipolar membrane electrolyser cell voltage, as well as the anode and cathode overpotentials.

This work shows that using electrocatalysts effectively decreases the cell voltage. This decrease is depending on the catalyst material and coating technique used. The bipolar membrane electrolyser cell voltage at $1000A/m^2$ and operated at $30.0\text{ }^\circ\text{C}$ in $1M\ Na_2SO_4$ at $\text{pH} = 13.4$ was found to be $3.66V$, while the use of electrocatalyst reduced this electrolyser cell voltage by $0.34V$.

A reduction both in cathode and anode overpotential was observed, indicating a more efficient system in oxygen and hydrogen production.

The lowest cell voltage at $1000A/m^2$ and operated at $30.0\text{ }^\circ\text{C}$ in $1M\ Na_2SO_4$ at $\text{pH} = 13.4$ was found be for the anode composed of *Ti*-mesh coated with platinum-Iridium oxide $10g/m^2$ as current collector, and contacted with five $175\mu\text{m}$ porous transport layers of sintered Titanium felt coated with *Ir- MMO*, while the cathode contained 1.4mm sintered *Ni*-felt coated with a *NiFeCo* dispersion and one layer of *Ni*-foam 0.3mm . The Ultraturrax was used for making the dispersion for the *NiFeCo* nanoparticle suspension with Nafion binder and some sodiumdodecylsulphate added. Flat platinized *Pt*-coated *Ti*-mesh 2.0 were used as current collector.

The four-hour runs were carried out at $1000A/m^2$ for bipolar membrane electrolysis controlled at $30.0\text{ }^\circ\text{C}$ using at start $1.0M\ NaOH$ as anolyte and $1.0\text{ M}\ Na_2SO_4$ as catholyte. The electrode dimensions were $10\text{cm} \times 10\text{cm}$ for the anode and the cathode. The pump speed of the anolyte and catholyte was $600\text{mL}/\text{min}$. At the beginning, the osmose cell, composed of a porous PTFE layer (POREX, PGM 25), was supplied with $0.5\text{ M}\ NaCl$ solution at one side pumped at $600\text{mL}/\text{min}$ and $600\text{mL}/\text{min}$ of catholyte of $1.0M\ Na_2SO_4$ at the other side of the POREX membrane. The bipolar membrane used was a symmetric FBM from Fumatech, Germany. With this bipolar membrane electrolysis stack, the cell voltage was lowered to $3.31 \pm 0.05V$ at $1000A/m^2$ at $30.0\text{ }^\circ\text{C}$ using electrocatalysts for the anode and cathode.

Even though progresses are constantly being made for direct seawater electrolysis for green hydrogen production, there are some challenges to the direct use of seawater. These challenges are mainly related to chloride and undesirable cations like Mg^{2+} , Ca^{2+} , and Sr^{2+} , commonly in seawater and they are the reason why only 4% of hydrogen is now being produced by electrolysis [2].

Although seawater is abundant in some regions, it is not a suitable feedstock for current electrolyser technologies due to the presence of electrochemically active anions like chloride that interfere with the oxygen evolution at the anode.

Moreover, the energy efficiency of the seawater electrolysis is also degraded by the presence of microorganisms and bacteria in the seawater, which reduce the long-term stability of the membranes. Another bottleneck hindering the progress of seawater electrolysis is the formation of insoluble precipitates on the cathode surface, which may poison the HER catalyst. This phenomenon is referred to as scaling and can be overcome using stable and corrosion resistant electrodes, as suggested by [34].

The hybrid setup for the DSWE used in this study, can be further improved to make the green hydrogen production from seawater safer, environmentally friendly and more efficient.

In particular, to make the electrolysis cell safer, it is possible to use pH-neutral solution as anolyte and catholyte. To test the postulate that a pH-neutral solution can be used both as an anolyte and catholyte for the bipolar membrane electrolysis, a sodium sulfate solution can be used as an electrolyte on both sides of the bipolar membrane. The postulate assumes that the BPM creates a local high pH at the AEL part of the BPM and a local low pH at the CEL part of the BPM. The local high pH value at the BPM's AEL part should allow even non-noble metals as electrocatalyst for the oxygen evolution reaction. Taking for the anolyte and catholyte a pH-neutral solution, like sodium sulfate, is safer both for the environment and the operator. To use sodium sulfate as an electrolyte, both for the anolyte and the catholyte, the temperature must be kept at $30\text{ }^\circ\text{C}$ due to the much lower solubility of sodium sulfate at temperatures below room temperature. As the sodium sulfate solution is not ultrapure, it can contain traces of *NaCl* that must be eliminated. To do so, the following three-step

purifying procedure for sodium sulphate solution was performed:

- Anion exchange resin IEX in OH^- form is transformed into SO_4^{2-} form [35] by mixing IEX in OH^- form with an excess of sodium sulfate.
- The sodium sulfate solution is purified ex-situ, preferably in a beaker glass with a mixer to prepare ultrapure sulfate solution from normal reagent grade sodium sulfate by adding IEX in OH^- form.
- By mixing the IEX, now in SO_4^{2-} form, with the reagent grade sodium sulfate at about 30 °C, possible traces of Cl^- are exchanged with the SO_4^{2-} from the IEX. The purified Na_2SO_4 solution can be used as anolyte and catholyte.

To make green hydrogen production using Direct seawater electrolysis with a BPM as a separator more sustainable, catalyst materials should not include noble metal compound, such as platinum based components.

The European Union target for the DSWE is to reach a cell voltage of 2.0V, at a current density of $5000A/m^2$ at 60.0 °C. However, in this thesis, the current density was limited to $1000A/m^2$ and 30.0 °C, due to the use of a commercial BPM from Fumatech, and maximum 40.0 °C.

A possibility to achieve current densities of even more than $1000A/m^2$, is to reduce the thickness of the BPM. However, this BPM thickness reduction can compromise the pH gradient's stability. A possible solution to this challenge would be the use of asymmetric BPMs. In an asymmetric BPM, the thickness of the two membrane layers differs, which allows for customization of the bipolar membrane properties. In future research, the substitution of the symmetric membrane with an asymmetric BPM holds great promise for achieving higher current densities, offering a promising way to enhance performance while ensuring pH stability through layer design and properties optimization.

Appendix

Bibliography

- [1] Zhijun Jia et al. “Blue energy: Current technologies for sustainable power generation from water salinity gradient”. In: *Renewable and Sustainable Energy Reviews* 31 (2014), pp. 91–100.
- [2] Siqi Jiang et al. “Recent advances in seawater electrolysis”. In: *Catalysts* 12.2 (2022), p. 123.
- [3] Ngai Yin Yip et al. “Salinity gradients for sustainable energy: primer, progress, and prospects”. In: *Environmental science & technology* 50.22 (2016), pp. 12072–12094.
- [4] Nahawand AlZainati et al. “Pressure retarded osmosis: Advancement, challenges and potential”. In: *Journal of Water Process Engineering* 40 (2021), p. 101950.
- [5] Ying Mei and Chuyang Y Tang. “Recent developments and future perspectives of reverse electro-dialysis technology: A review”. In: *Desalination* 425 (2018), pp. 156–174.
- [6] Raúl A Rica et al. “Capacitive mixing for harvesting the free energy of solutions at different concentrations”. In: *Entropy* 15.4 (2013), pp. 1388–1407.
- [7] Ngai Yin Yip and Menachem Elimelech. “Comparison of energy efficiency and power density in pressure retarded osmosis and reverse electro-dialysis”. In: *Environmental science & technology* 48.18 (2014), pp. 11002–11012.
- [8] Fei Liu et al. “Parallel up-scaling of Capacitive Mixing (CapMix) system enhances the specific performance”. In: *Electrochimica Acta* 187 (2016), pp. 104–112.
- [9] Shanxue Jiang et al. “A comprehensive review on the synthesis and applications of ion exchange membranes”. In: *Chemosphere* 282 (2021), p. 130817.
- [10] Alessandro Pedico et al. “Green methods for the fabrication of graphene oxide membranes: from graphite to membranes”. In: *Membranes* 13.4 (2023), p. 429.
- [11] Mine Eti et al. “Ion exchange membranes for reverse electro-dialysis (RED) applications-recent developments”. In: *Journal of Membrane Science and Research* 7.4 (2021), pp. 260–267.
- [12] Chalida Klaysom et al. “Preparation of porous ion-exchange membranes (IEMs) and their characterizations”. In: *Journal of membrane science* 371.1-2 (2011), pp. 37–44.
- [13] Shanxue Jiang and Bradley P Ladewig. “Green synthesis of polymeric membranes: Recent advances and future prospects”. In: *Current Opinion in Green and Sustainable Chemistry* 21 (2020), pp. 1–8.
- [14] Tongwen Xu. “Ion exchange membranes: State of their development and perspective”. In: *Journal of membrane science* 263.1-2 (2005), pp. 1–29.
- [15] Chen Shen and S Olutunde Oyadiji. “The processing and analysis of graphene and the strength enhancement effect of graphene-based filler materials: A review”. In: *Materials Today Physics* 15 (2020), p. 100257.
- [16] Jingyi Wang et al. “Aramid nanofibers/reduced graphene oxide composite electrodes with high mechanical properties”. In: *Nanomaterials* 13.1 (2022), p. 103.

-
- [17] J Niklas Hausmann et al. “Is direct seawater splitting economically meaningful?” In: *Energy & Environmental Science* 14.7 (2021), pp. 3679–3685.
- [18] Jiaxin Guo et al. “Direct seawater electrolysis by adjusting the local reaction environment of a catalyst”. In: *Nature Energy* 8.3 (2023), pp. 264–272.
- [19] Abdulhai H Faqeeh and Mark D Symes. “Zero-Gap Bipolar Membrane Water Electrolyzers: Principles, Challenges and Practical Insights”. In: *Electrochimica Acta* (2024), p. 144345.
- [20] R Pärnamäe et al. “Bipolar membranes: A review on principles, latest developments, and applications”. In: *Journal of Membrane Science* 617 (2021), p. 118538.
- [21] Britta Mayerhöfer et al. “Bipolar membrane electrode assemblies for water electrolysis”. In: *ACS applied energy materials* 3.10 (2020), pp. 9635–9644.
- [22] Sören Drespe et al. “Direct electrolytic splitting of seawater: opportunities and challenges”. In: *ACS Energy Letters* 4.4 (2019), pp. 933–942.
- [23] Vasil Bachvarov, Elefteria Lefterova, and Rashko Rashkov. “Electrodeposited NiFeCo and NiFe-CoP alloy cathodes for hydrogen evolution reaction in alkaline medium”. In: *international journal of hydrogen energy* 41.30 (2016), pp. 12762–12771.
- [24] Heping Xie et al. “A membrane-based seawater electrolyser for hydrogen generation”. In: *Nature* 612.7941 (2022), pp. 673–678.
- [25] Anna Aixalà-Perelló et al. “Enhancing Surface Charge Density of Graphene Oxide Membranes through Al (OH)⁴⁻ Anion Incorporation for Osmotic Energy Conversion”. In: *Advanced Energy and Sustainability Research* 5.9 (2024), p. 2400090.
- [26] Xiaoyan Hu et al. “Nickel foam and stainless steel mesh as electrocatalysts for hydrogen evolution reaction, oxygen evolution reaction and overall water splitting in alkaline media”. In: *RSC advances* 9.54 (2019), pp. 31563–31571.
- [27] Anna Aixalà-Perelló et al. “Scalable and highly selective graphene-based ion-exchange membranes with tunable permselectivity”. In: *npj 2D Materials and Applications* 7.1 (2023), p. 46.
- [28] Janghoon Park, Keehyun Shin, and Changwoo Lee. “Roll-to-roll coating technology and its applications: A review”. In: *International Journal of Precision Engineering and Manufacturing* 17 (2016), pp. 537–550.
- [29] Janghoon Park et al. “Roll-to-roll production of catalyst coated membranes for low-temperature electrolyzers”. In: *Journal of Power Sources* 479 (2020), p. 228819.
- [30] Julia Van Drunen et al. “Electrochemically active nickel foams as support materials for nanoscopic platinum electrocatalysts”. In: *ACS applied materials & interfaces* 6.15 (2014), pp. 12046–12061.
- [31] Dandan Guo et al. “Self-supporting NiFe layered double hydroxide “Nanoflower” cluster anode electrode for an efficient alkaline anion exchange membrane water electrolyzer”. In: *Energies* 15.13 (2022), p. 4645.
- [32] Christomir Christov and Nancy Moller. “Chemical equilibrium model of solution behavior and solubility in the H-Na-K-OH-Cl-HSO₄-SO₄-H₂O system to high concentration and temperature”. In: *Geochimica et Cosmochimica Acta* 68.6 (2004), pp. 1309–1331.
- [33] HK Abdel-Aal, KM Zohdy, and M Abdel Kareem. “Hydrogen production using sea water electrolysis”. In: *The Open Fuel Cells Journal* 3.1 (2010), pp. 1–7.
- [34] Li Zhao et al. “Design strategy of corrosion-resistant electrodes for seawater electrolysis”. In: *Materials* 16.7 (2023), p. 2709.
- [35] Edward A Kyser. “Flowsheet for Conversion of Anion Resin from Nitrate to Sulfate form for Disposal”. In: (2021).